Supplementary Information (SI) for Dalton Transactions.
This journal is © The Royal Society of Chemistry 2024

Supporting Information for: Electroanalytical Characterization of Np(VI)/Np(V) Redox in a Pentadentate Ligand Environment and Stabilization of $[Np^{V}O_2]^+$ by Hydrogen Bonding

Emily R. Mikeska,[†,‡] T. Davis Curry,[†] Richard E. Wilson,[*,‡] and James D. Blakemore[*,†]

†*Department of Chemistry, University of Kansas, 1567 Irving Hill Road, Lawrence, KS 66045*

‡*Chemical Sciences and Engineering Division, Argonne National Laboratory, Lemont, IL 60439*

E-mail: rewilson@anl.gov; blakemore@ku.edu

Contents

1 Electrochemistry

Eq. 1: Expression for the ratio of the anodic current at the end of the backward potential step to the cathodic current at the end of the forward potential step in double potential step chronoamperometry when the system displays complete chemical reversibility. The current measurements are accomplished experimentally by initializing the cell at a potential where no electrochemical processes are occurring. To probe a reduction process and the related return oxidation, one potential step is taken at time $t = 0$ to a negative potential significantly beyond that needed to accomplish the reduction such that the driving force for electron transfer is large and the system is only diffusion limited. The potential is held (typically between 250 μs - 1s; denoted here as t_R) followed by a single potential step is taken back to the original rest potential (which is held for the same amount of time as the forward step; denoted $2t_R$).

$$\frac{-i_a(2t_R)}{i_c(t_R)} = 1 - \frac{1}{\sqrt{2}} \tag{1}$$

Eq. 2: Expression for the degree of chemical reversibility, where $\mathrm{R}_{DPS} = 1$ for a fully reversible system.

$$R_{DPS} = \frac{-i_a(2t_R)/i_c(t_R)}{1 - 1/\sqrt{2}} \tag{2}$$

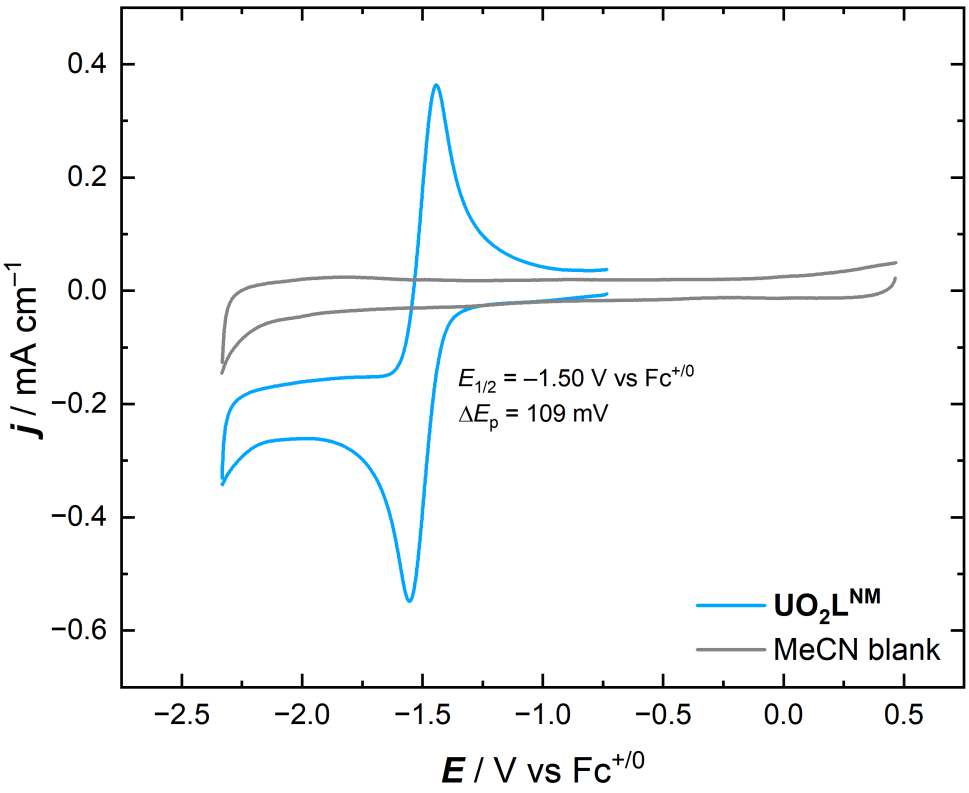

Figure S1: Cyclic voltammetry data for $\mathbf{UO_2L}^{NM}$ in CH_3CN/$TBAPF_6$ and a blank CV of CH_3CN/$TBAPF_6$, collected after 5 minutes of sparging with N_2. Conditions: [U] = 1 mM, scan rate = 100 mV/s.

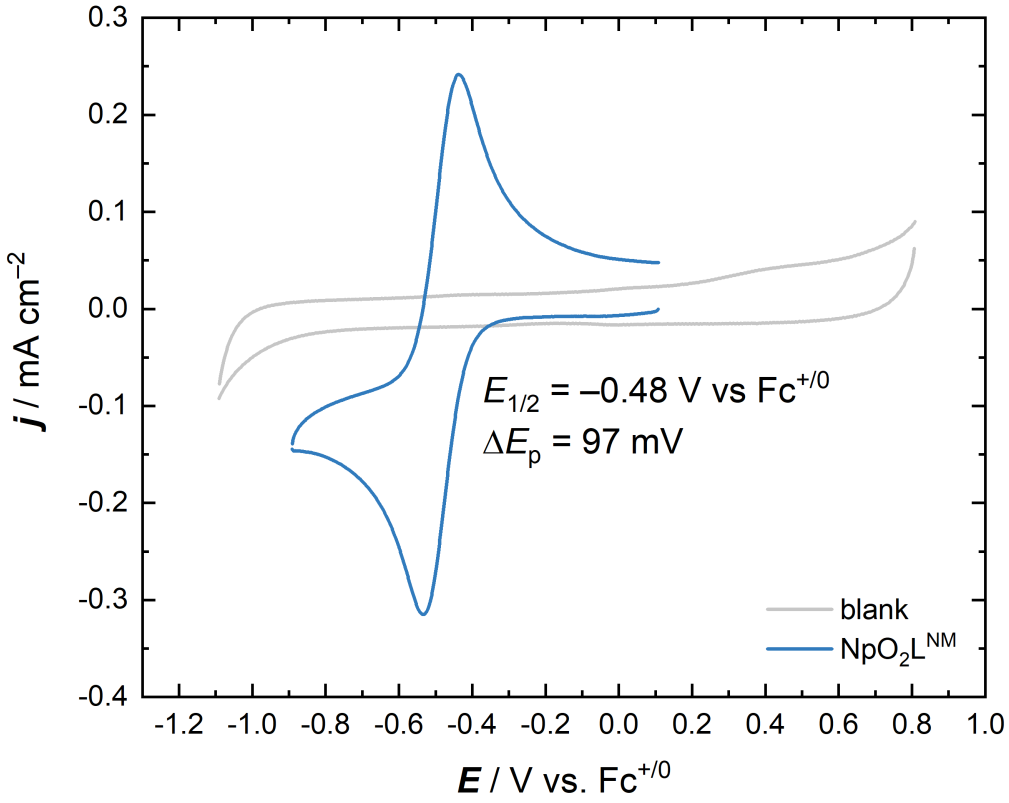

Figure S2: Overlay of voltammetry for $\mathbf{NpO_2L}^{NM}$ in $CH_3CN/TBAPF_6$ and a blank CV of $CH_3CN/TBAPF_6$. Conditions: [Np] = 1 mM, scan rate = 100 mV/s.

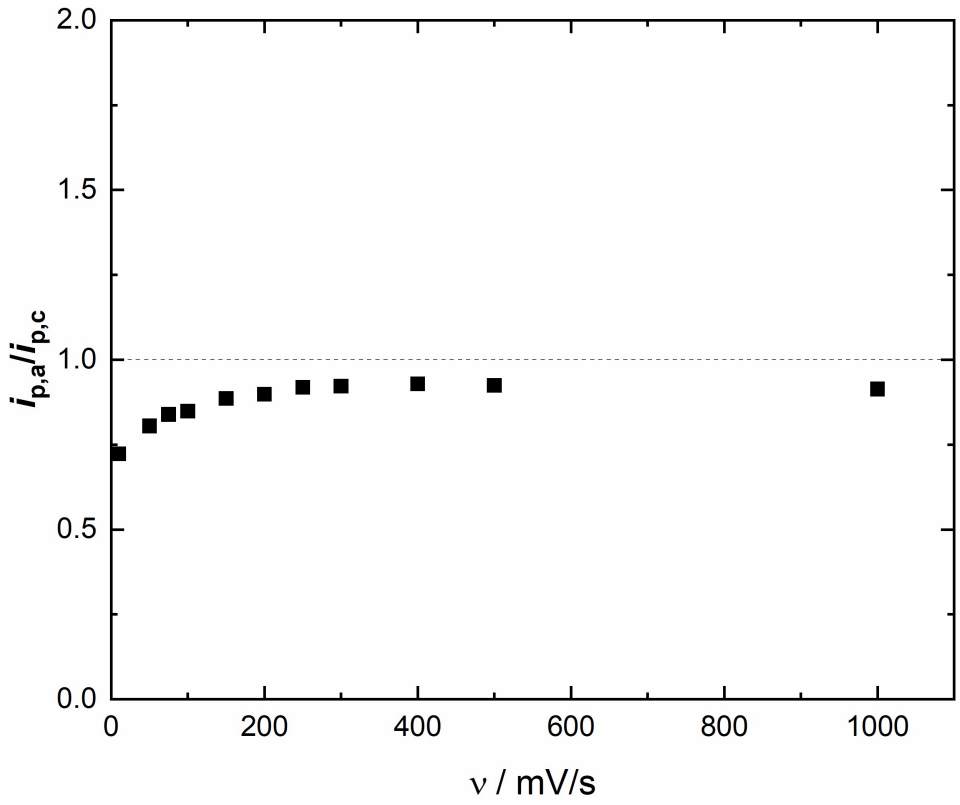

Figure S3: Ratio of peak anodic and peak cathodic currents corresponding to the Np(VI/V) couple measured in CH_3CN/$TBAPF_6$. The process being interrogated is shown in Figure S2. Peak currents were background subtracted using standard methods. Note that a peak current ratio of 1 corresponds to a chemically reversible process in which the reduced form is stable in solution.

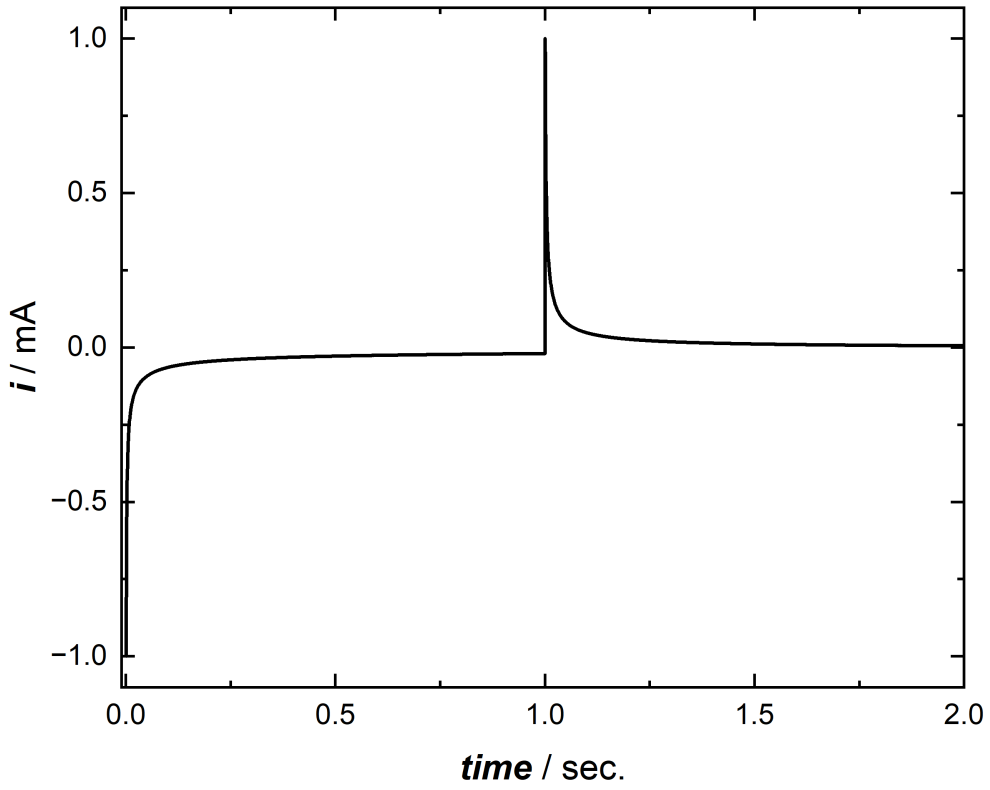

Figure S4: Potential waveform for double potential step chronoamperometry of $\mathbf{NpO_2L}^{NM}$ in $CH_3CN/TBAPF_6$. Conditions: [Np] = 1 mM; initial potential: –0.08 V vs $Fc^{+/0}$, forward step potential: –0.93 V vs $Fc^{+/0}$, backward step potential –0.08 V vs $Fc^{+/0}$.

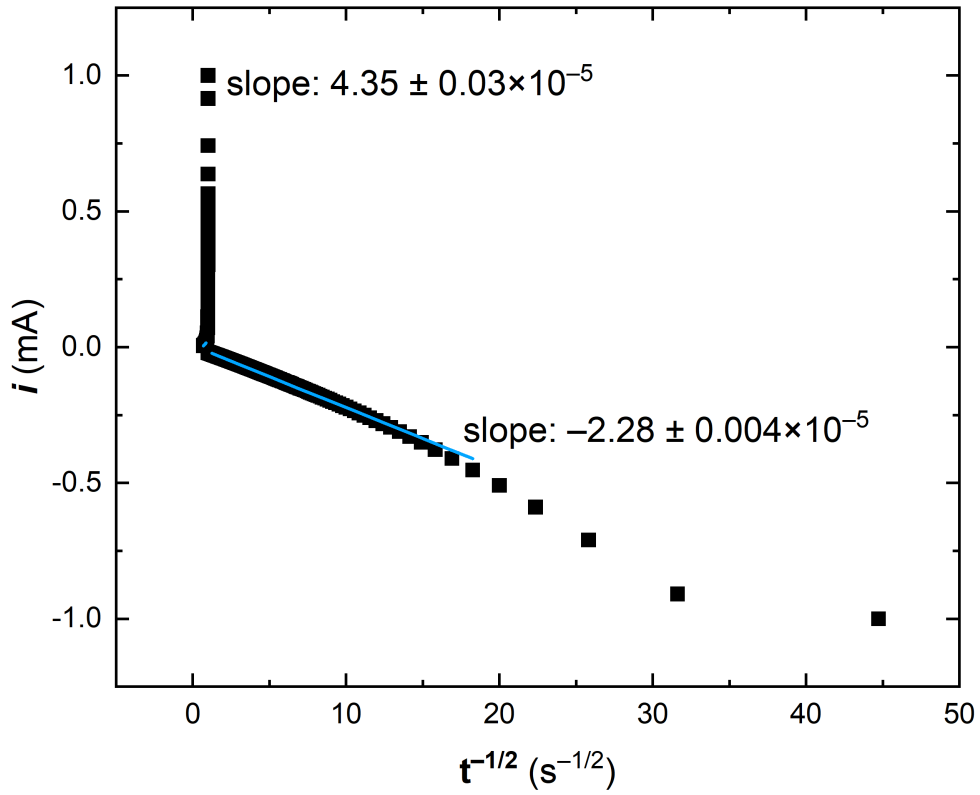

Figure S5: Cottrell plot for $\mathbf{NpO_2L}^{NM}$ in CH_3CN/$TBAPF_6$. The slope of the fitted line was used to experimentally determine D_{ox} and D_{red} in Table 1 of the main text.

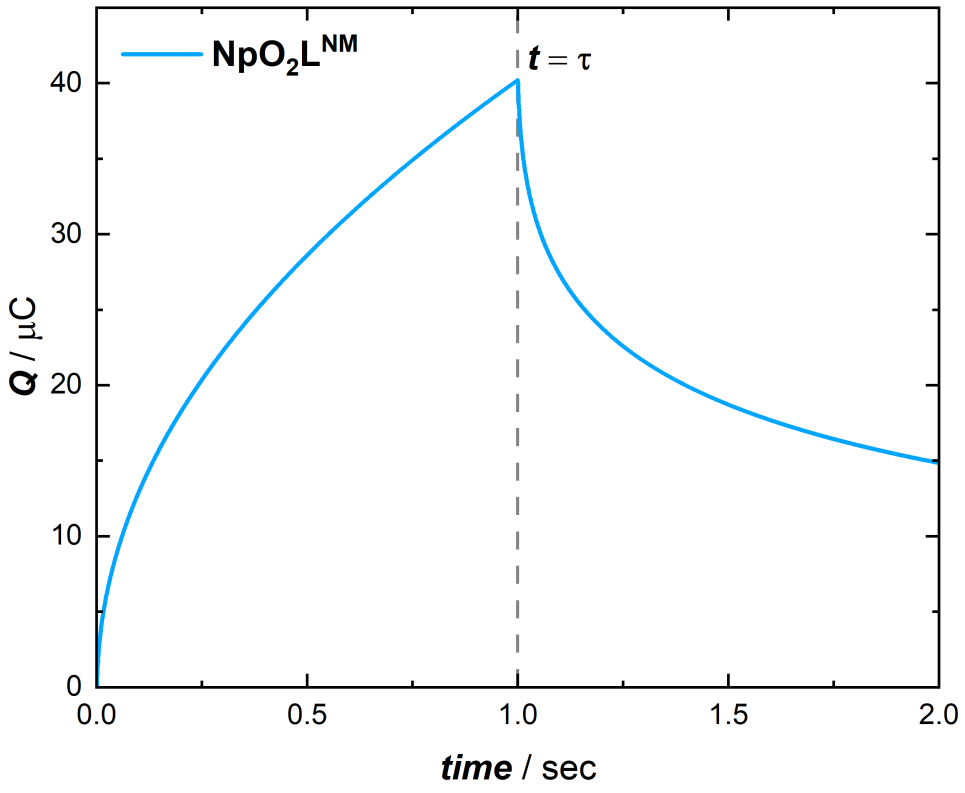

Figure S6: Double potential step chronocoulometry of $\mathbf{NpO_2L}^{NM}$ in CH_3CN/$TBAPF_6$ obtained from integration of the double potential step chronoamperometry data given above. Charge-time curve for the potential steps from –0.08 V to –0.93 V vs $Fc^{+/0}$ and –0.93 V to –0.08 V vs $Fc^{+/0}$. The time point of the switching potential is denoted τ.

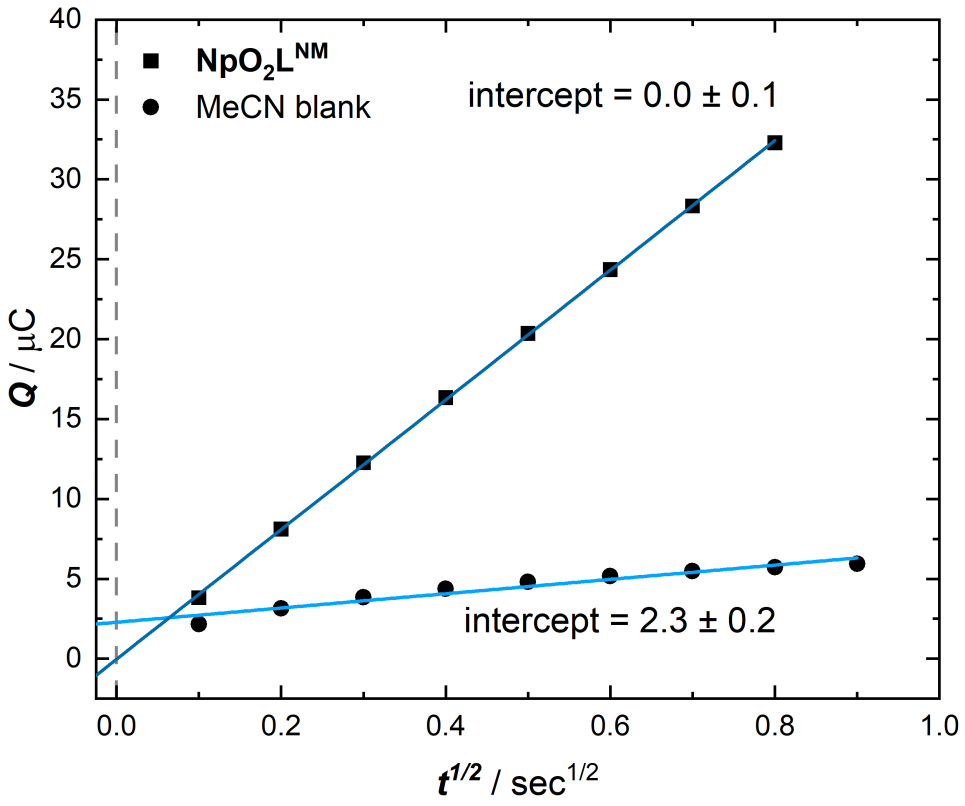

Figure S7: Chronocoulometry of $\mathbf{NpO_2L}^{NM}$ in CH_3CN/$TBAPF_6$. Plot of the integrated Cottrell equation (charge vs. $t^{1/2}$) for the first potential step (–0.08 V to –0.93 V vs $Fc^{+/0}$), showing that the intercepts of lines for $\mathbf{NpO_2L}^{NM}$ in CH_3CN/$TBAPF_6$ and the background electrolyte are within 3 $\mu C/cm^2$ of each other. This good agreement of the intercepts indicates that the oxidized form of the compound does not adsorb to the electrode surface in CH_3CN electrolyte.[1]

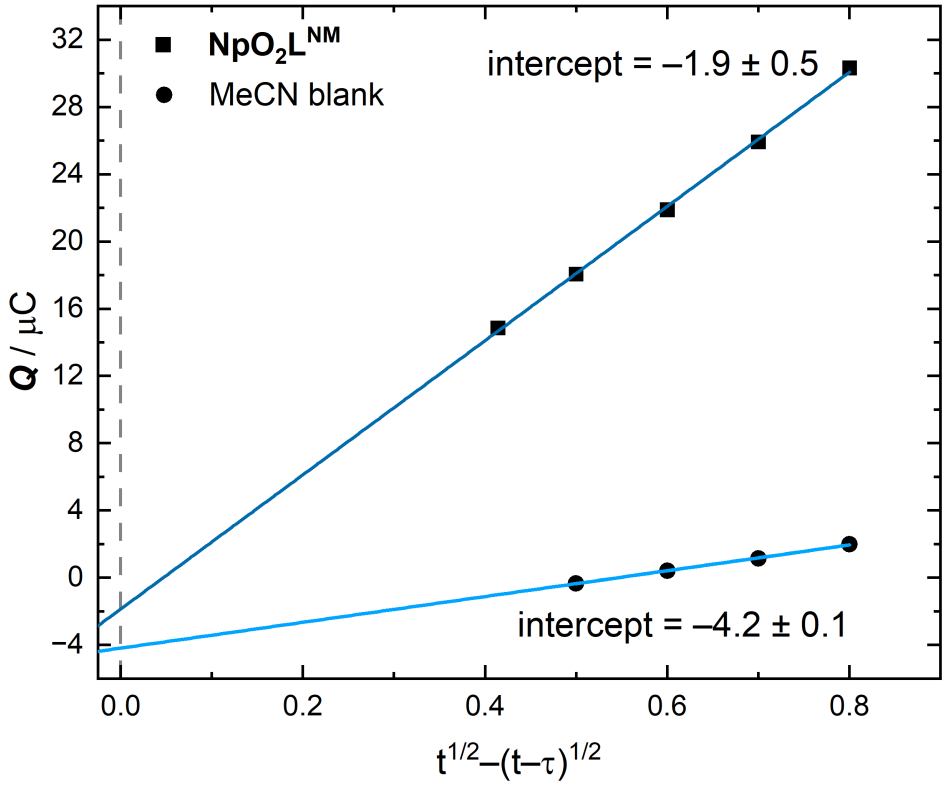

Figure S8: Chronocoulometry of $\mathbf{NpO_2L}^{NM}$ in CH_3CN/$TBAPF_6$. Plot of the integrated Cottrell equation (charge (at $t > \tau$) vs. $[t^{1/2}\text{-}(t\text{-}\tau)^{1/2}]$) for the second potential step (–0.93 V to –0.08 V vs $Fc^{+/0}$), showing that the intercepts of lines for $\mathbf{NpO_2L}^{NM}$ in CH_3CN/$TBAPF_6$ and the background electrolyte are within 3 $\mu C/cm^2$ of each other. This good agreement of the intercepts indicates that the reduced form of the compound does not adsorb to the electrode surface in CH_3CN electrolyte.[1]

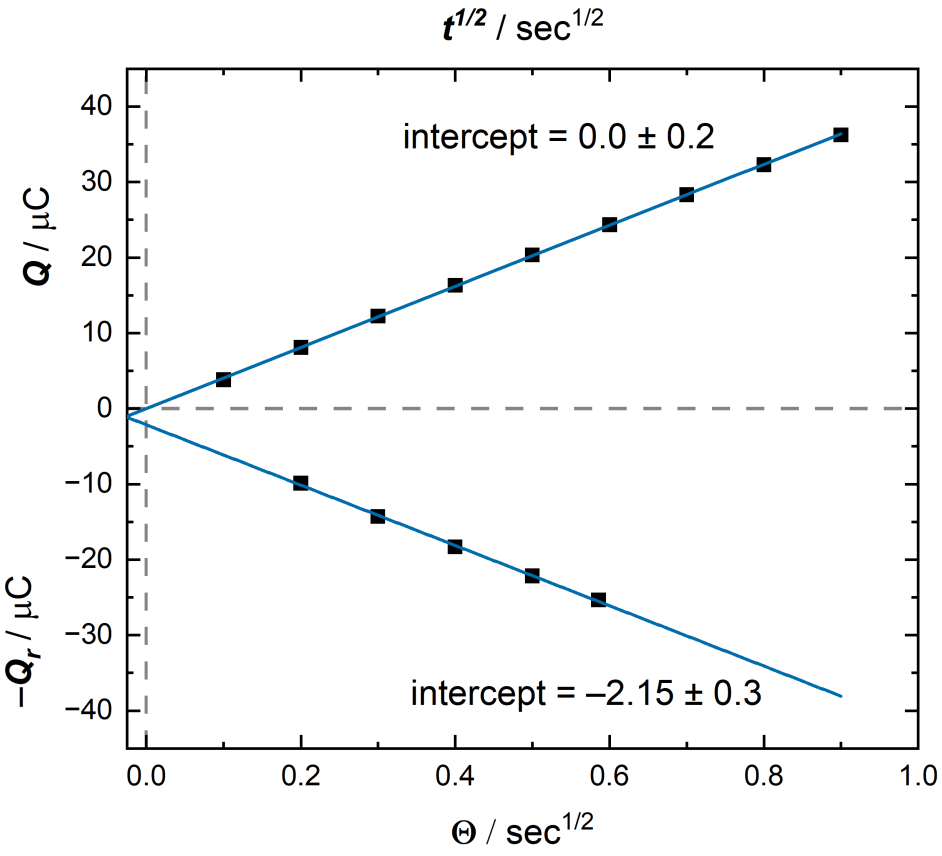

Figure S9: Chronocoulometry of $\mathbf{NpO_2L}^{NM}$ in CH_3CN/$TBAPF_6$. Top x-axis: Plot of the integrated Cottrell equation (charge vs. $t^{1/2}$) for the first potential step (–0.08 V to –0.93 V vs $Fc^{+/0}$). Bottom x-axis: Plot of the integrated Cottrell equation (Q_r vs. Θ) for the second potential step (–0.93 V to –0.08 V vs $Fc^{+/0}$), adjusted by τ, where $Q_r = Q_\tau – Q(t>\tau)$ and $\Theta = [\tau^{1/2} + (t–\tau)^{1/2} – t^{1/2}]$. The intercepts of the lines for both potential steps are within 3 $\mu C/cm^2$ of each other and within 3 $\mu C/cm^2$ of 0.[1]

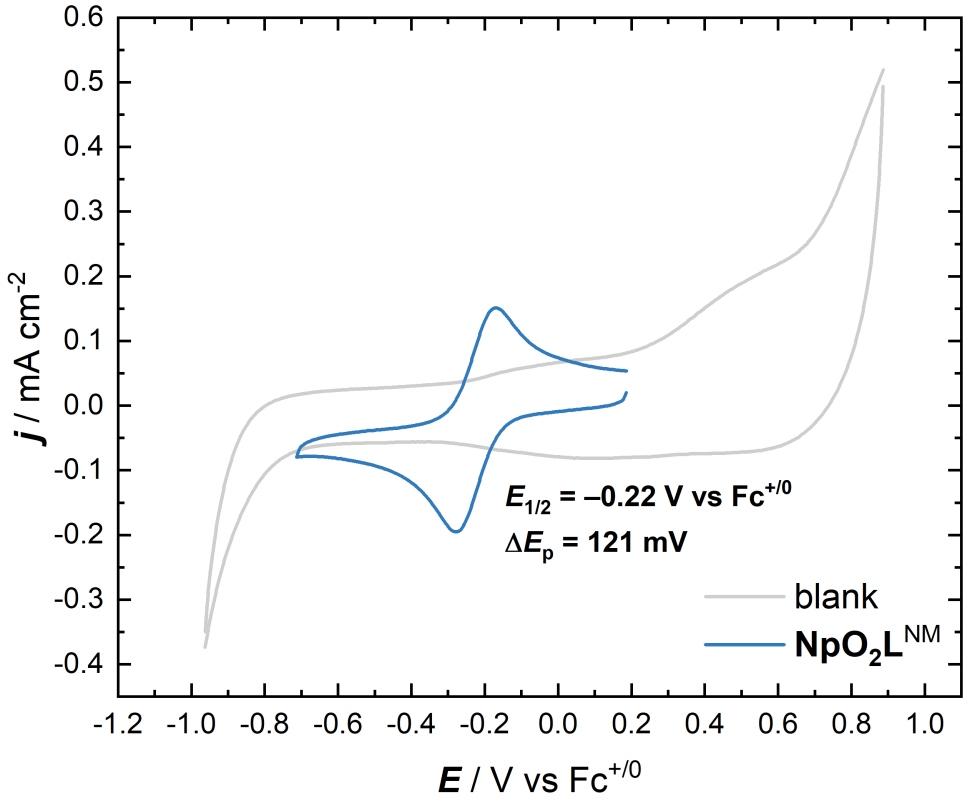

Figure S10: Overlay of voltammetry for $\mathbf{NpO_2L}^{NM}$ in $CH_3OH/TBAPF_6$ and a blank CV of $CH_3OH/TBAPF_6$, showing the above background current from the solvent and the proximity of the couple from $\mathbf{NpO_2L}^{NM}$ to the solvent wall. Conditions: [Np] = 1 mM, scan rate = 100 mV/s.

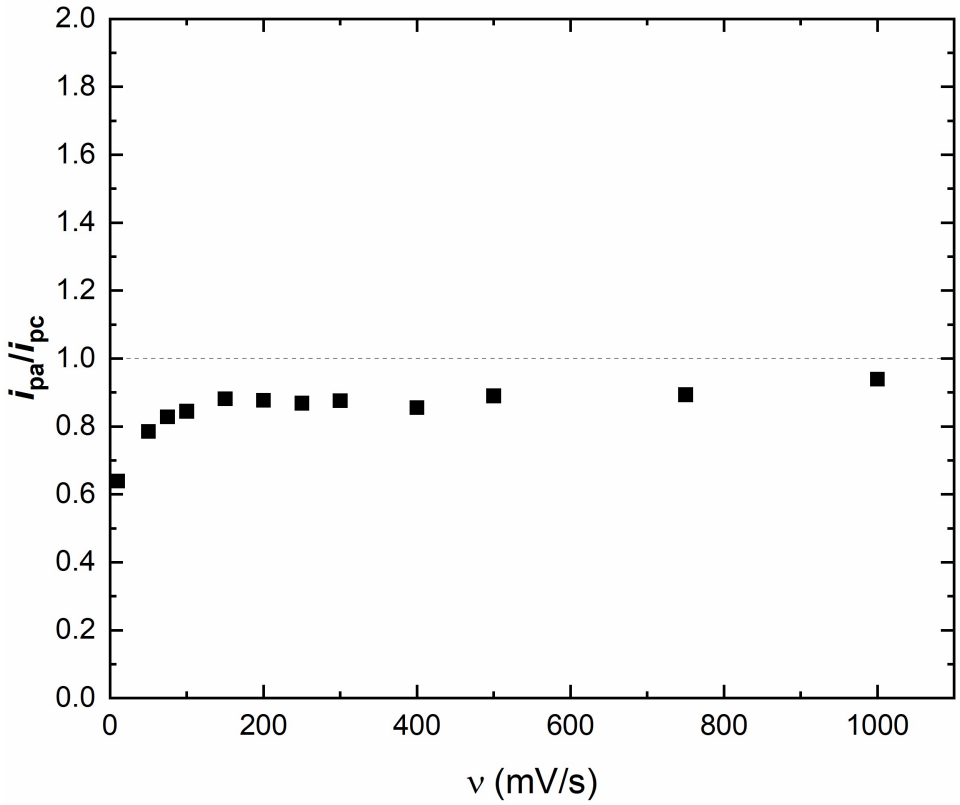

Figure S11: Ratio of peak anodic and peak cathodic currents corresponding to the Np(VI/V) couple measured in CH_3OH/$TBAPF_6$. The process being interrogated is shown in Figure S10. Peak currents were background subtracted using standard methods. Note that a peak current ratio of 1 corresponds to a chemically reversible process in which the reduced form is stable in solution.

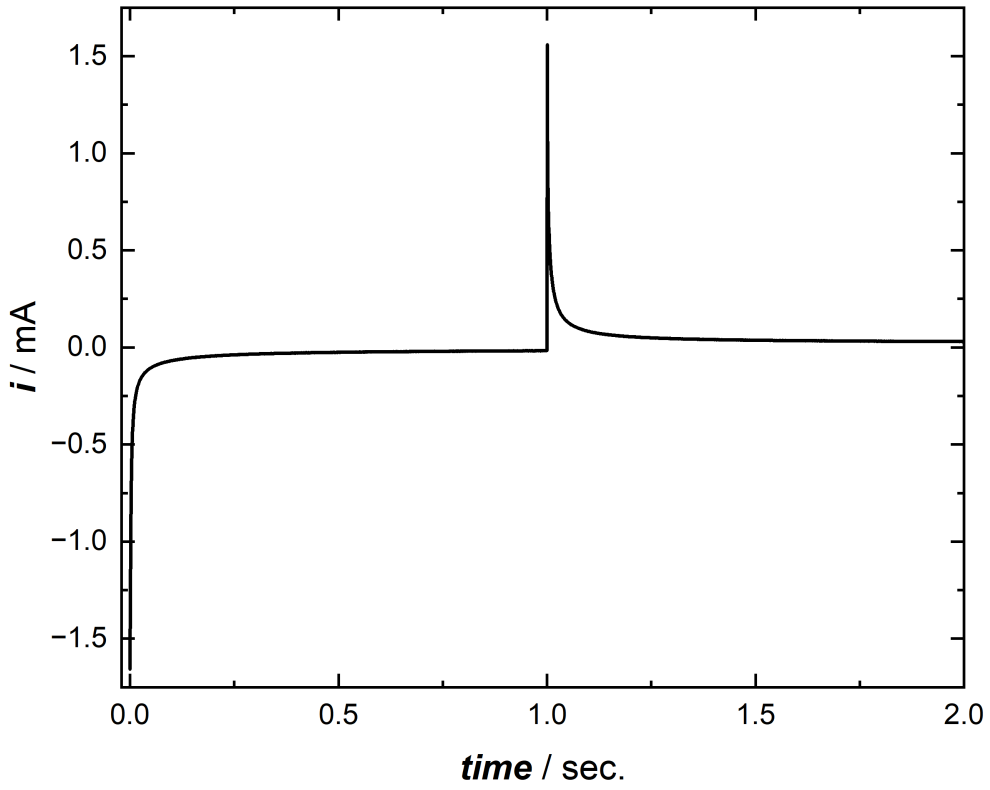

Figure S12: Potential waveform for double potential step chronoamperometry of $\mathbf{NpO_2L}^{NM}$ in $CH_3OH/TBAPF_6$. Conditions: [Np] = 1 mM; initial potential: 0.11 V vs $Fc^{+/0}$, forward step potential: –0.71 V vs $Fc^{+/0}$, backward step potential 0.11 V vs $Fc^{+/0}$.

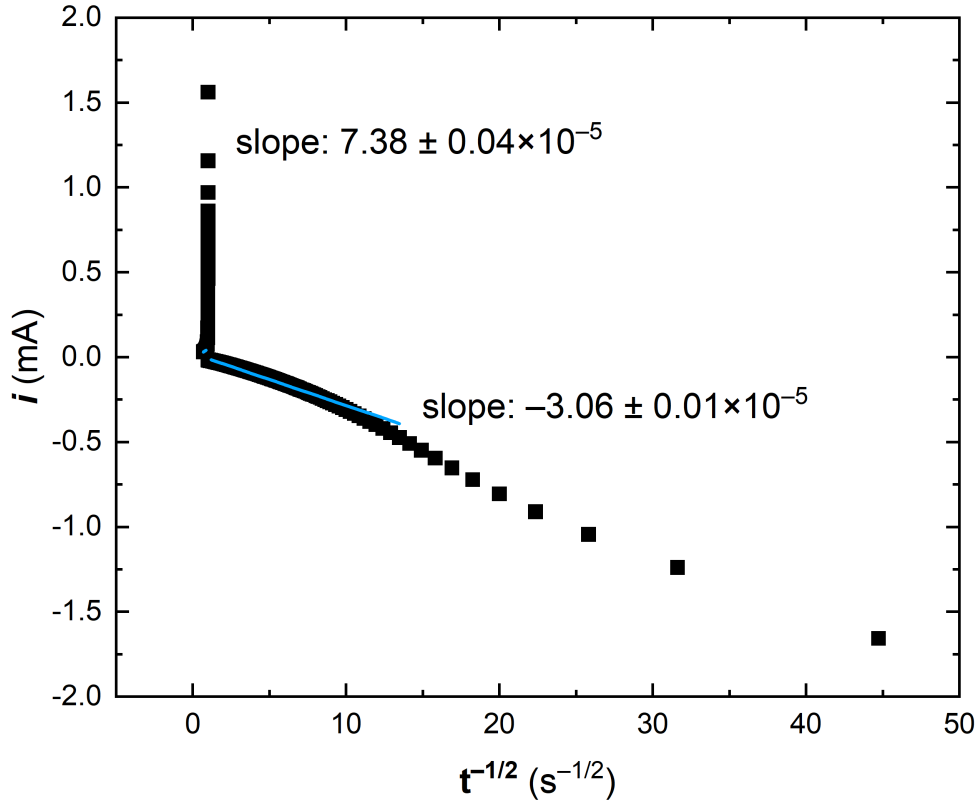

Figure S13: Cottrell plot for $\mathbf{NpO_2L}^{NM}$ in CH_3OH/$TBAPF_6$. The slope of the fitted line was used to experimentally determine D_{ox} and D_{red} in Table 1 of the main text

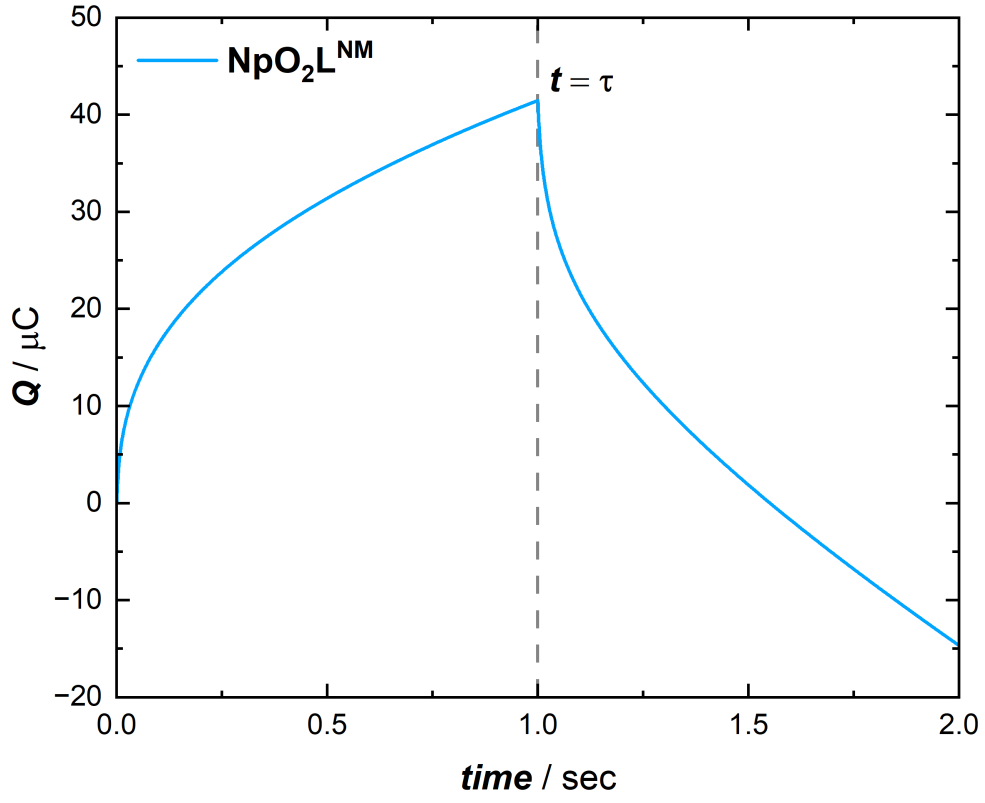

Figure S14: Double potential step chronocoulometry of $\mathbf{NpO_2L}^{NM}$ in $CH_3OH/TBAPF_6$ obtained from integration of the double potential step chronoamperometry data given above. Charge-time curve for the potential steps from 0.11 V to –0.71 V vs $Fc^{+/0}$ and –0.71 V to 0.11 V vs $Fc^{+/0}$. The time point of the switching potential is denoted τ.

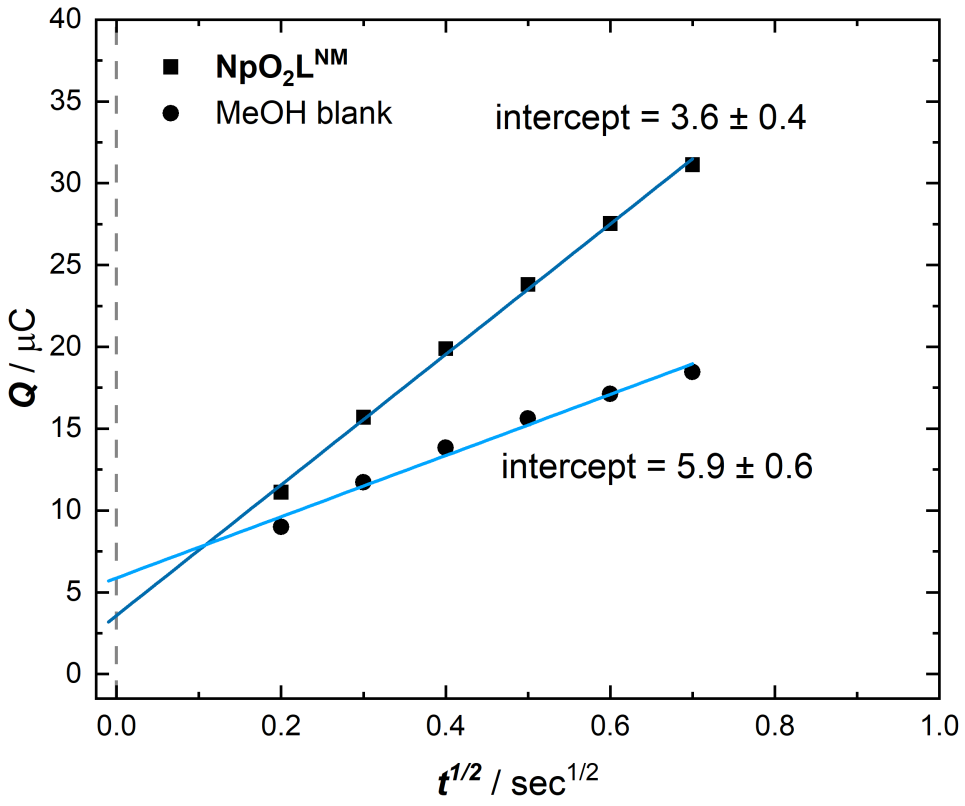

Figure S15: Chronocoulometry of $\mathbf{NpO_2L}^{NM}$ in CH_3OH/$TBAPF_6$. Plot of the integrated Cottrell equation (charge vs. $t^{1/2}$) for the first potential step (0.11 V to –0.71 V vs $Fc^{+/0}$), showing that the intercepts of lines for $\mathbf{NpO_2L}^{NM}$ in CH_3OH/$TBAPF_6$ and the background electrolyte are within 3 $\mu C/cm^2$ of each other. This good agreement of the intercepts indicates that the oxidized form of the compound does not adsorb to the electrode surface in CH_3OH electrolyte.[1]

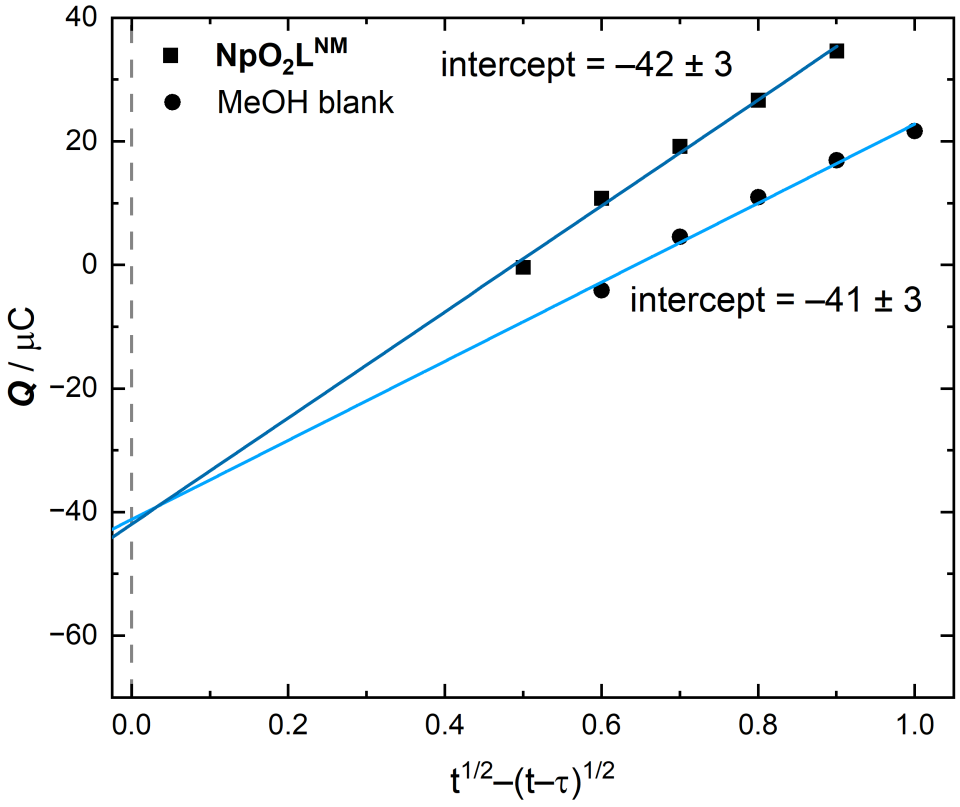

Figure S16: Chronocoulometry of $\mathbf{NpO_2L}^{NM}$ in CH_3OH/$TBAPF_6$. Plot of the integrated Cottrell equation (charge (at $t > \tau$) vs. $[t^{1/2}\text{-}(t\text{-}\tau)^{1/2}]$) for the second potential step (–0.71 V to 0.11 V vs $Fc^{+/0}$), showing that the intercepts of lines for $\mathbf{NpO_2L}^{NM}$ in CH_3OH/$TBAPF_6$ and the background electrolyte are within 3 $\mu C/cm^2$ of each other. This good agreement of the intercepts indicates that the reduced form of the compound does not adsorb to the electrode surface in CH_3OH electrolyte.[1]

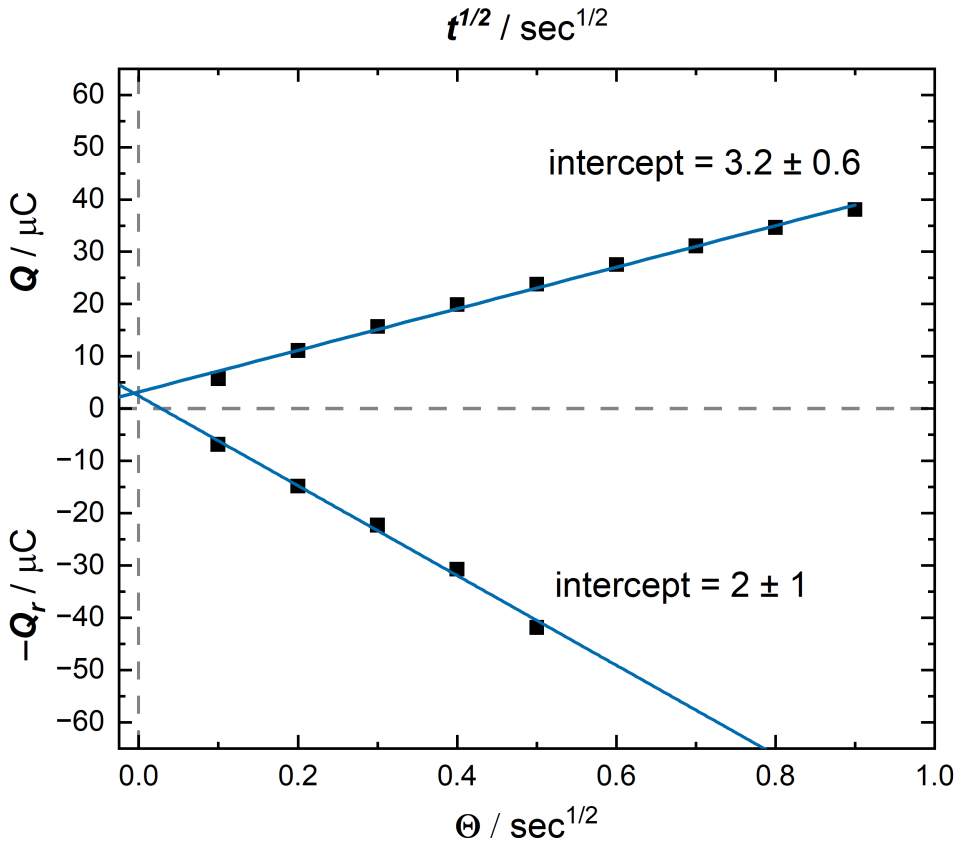

Figure S17: Chronocoulometry of $\mathbf{NpO_2L}^{NM}$ in CH_3CN/$TBAPF_6$. Top x-axis: Plot of the integrated Cottrell equation (charge vs. $t^{1/2}$) for the first potential step (0.11 V to –0.71 V vs $Fc^{+/0}$). Bottom x-axis: Plot of the integrated Cottrell equation (Q_r vs. Θ) for the second potential step (–0.71 V to 0.11 V vs $Fc^{+/0}$), adjusted by τ, where $Q_r = Q_\tau - Q(t>\tau)$ and $\Theta = [\tau^{1/2} + (t-\tau)^{1/2} - t^{1/2}]$. The intercepts of the lines for both potential steps are within 3 $\mu C/cm^2$ of each other and within 3 $\mu C/cm^2$ of 0.[1]

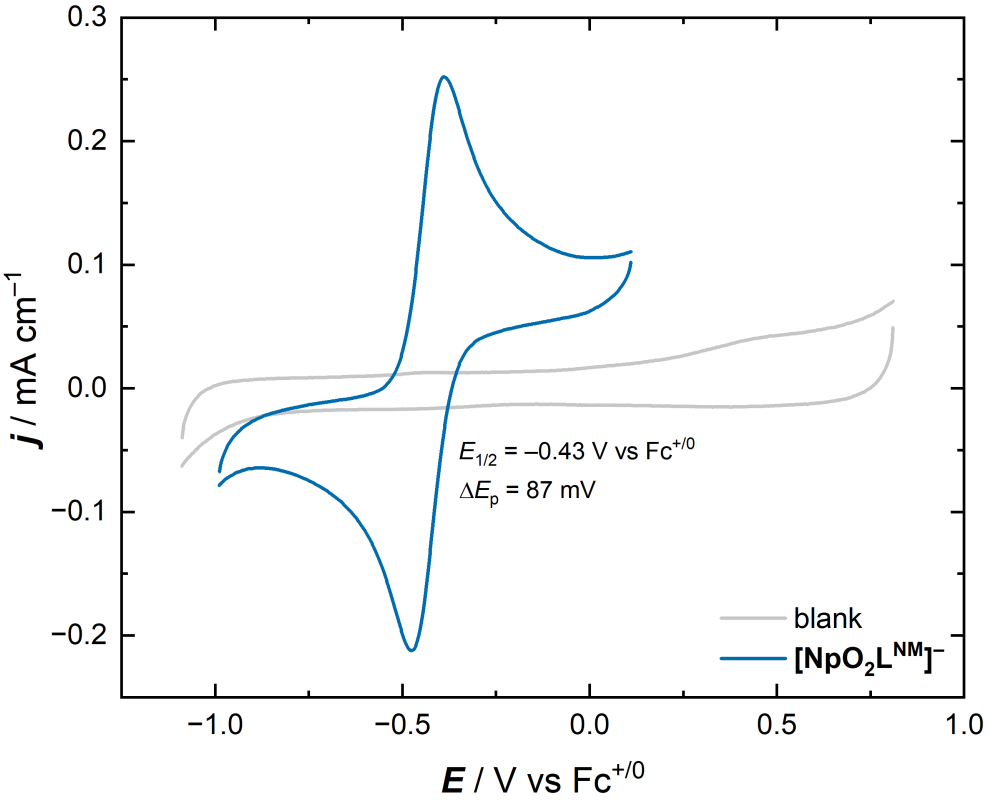

Figure S18: Overlay of voltammetry for $\mathbf{[NpO_2L^{NM}]^-}$ in 0.2 M $TBAPF_6$ in CH_3CN and a blank CV of 0.2 M $TBAPF_6$ in CH_3CN. Conditions: [Np] = 1.1 mM in 0.2 M $TBAPF_6$ in MeCN, scan rate = 100 mV/s.

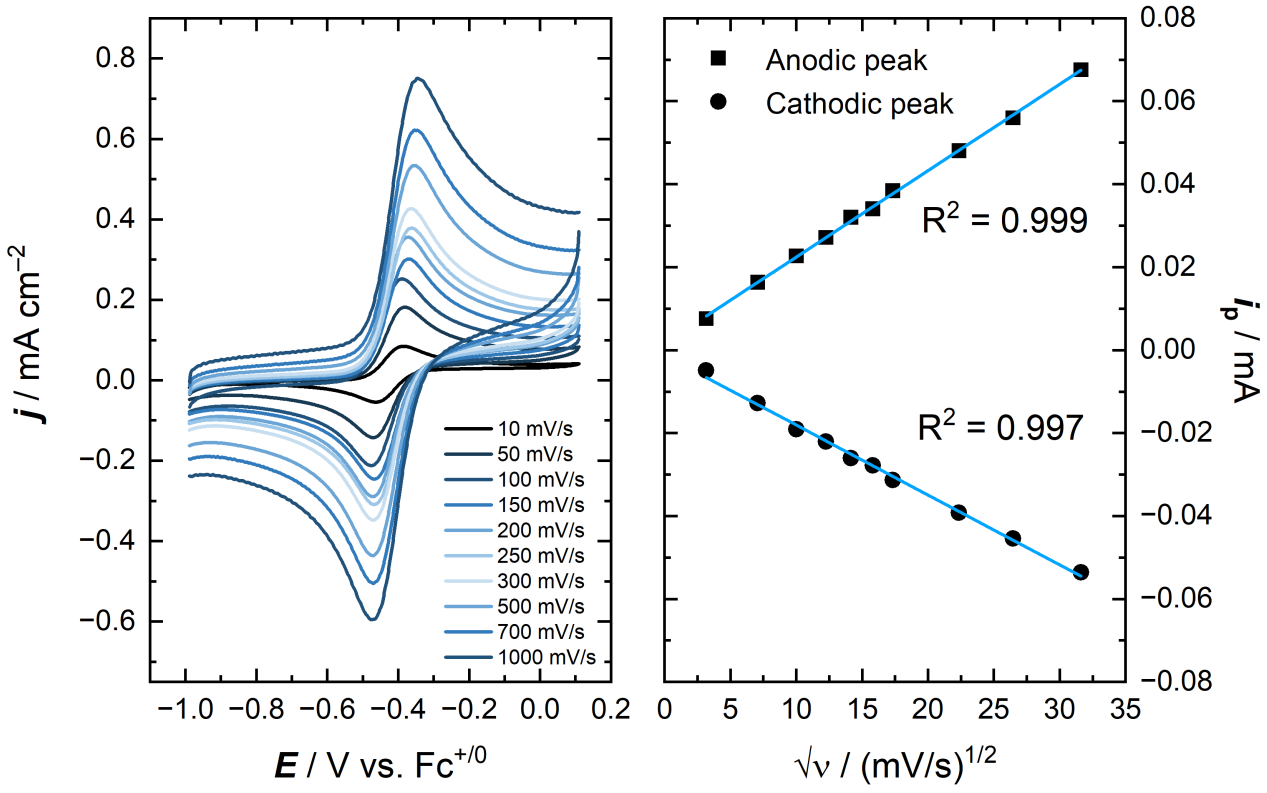

Figure S19: Left: Scan rate-dependent data for $\mathbf{[NpO_2L}^{NM}\mathbf{]}^-$ in 0.2 M $TBAPF_6$ in CH_3CN. Right: Plot of peak current vs (scan rate)$^{1/2}$, demonstrating the diffusional nature of the reduced and oxidized species. Conditions: [Np] = 1.1 mM.

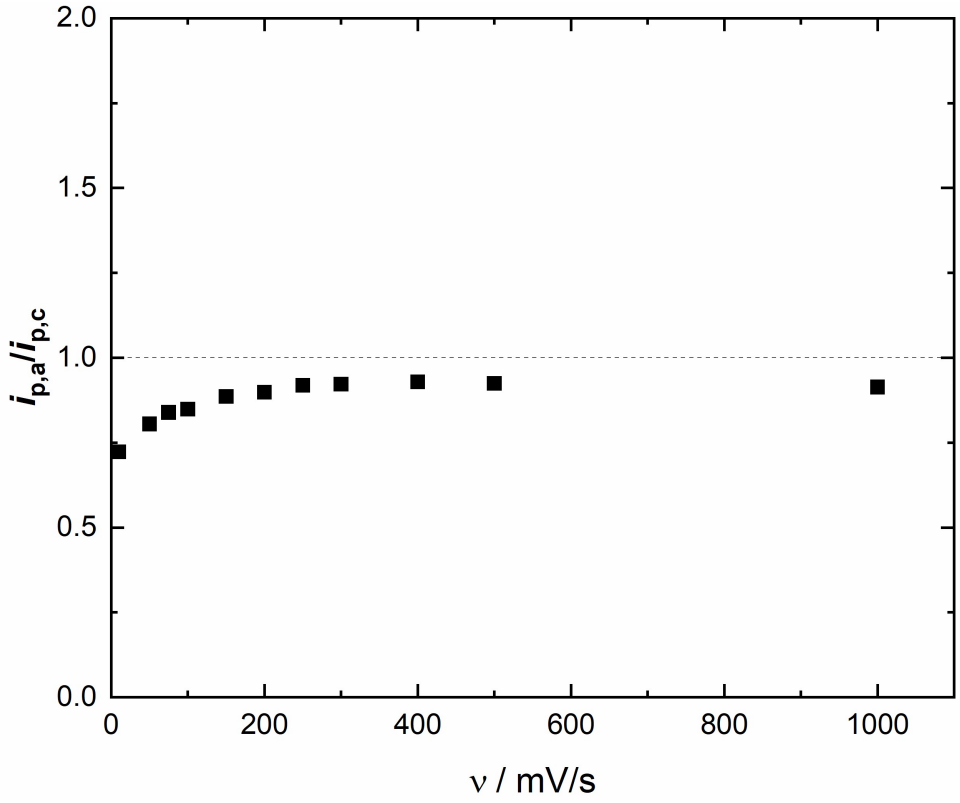

Figure S20: Ratio of peak anodic and peak cathodic currents corresponding to the Np(VI/V) couple measured for $\mathbf{[NpO_2L}^{NM}\mathbf{]}^-$ in 0.2 M $TBAPF_6$ in CH_3CN. The process being interrogated is that shown in Figure S18. Peak currents were background subtracted using standard methods.

2 Electrochemical Simulations

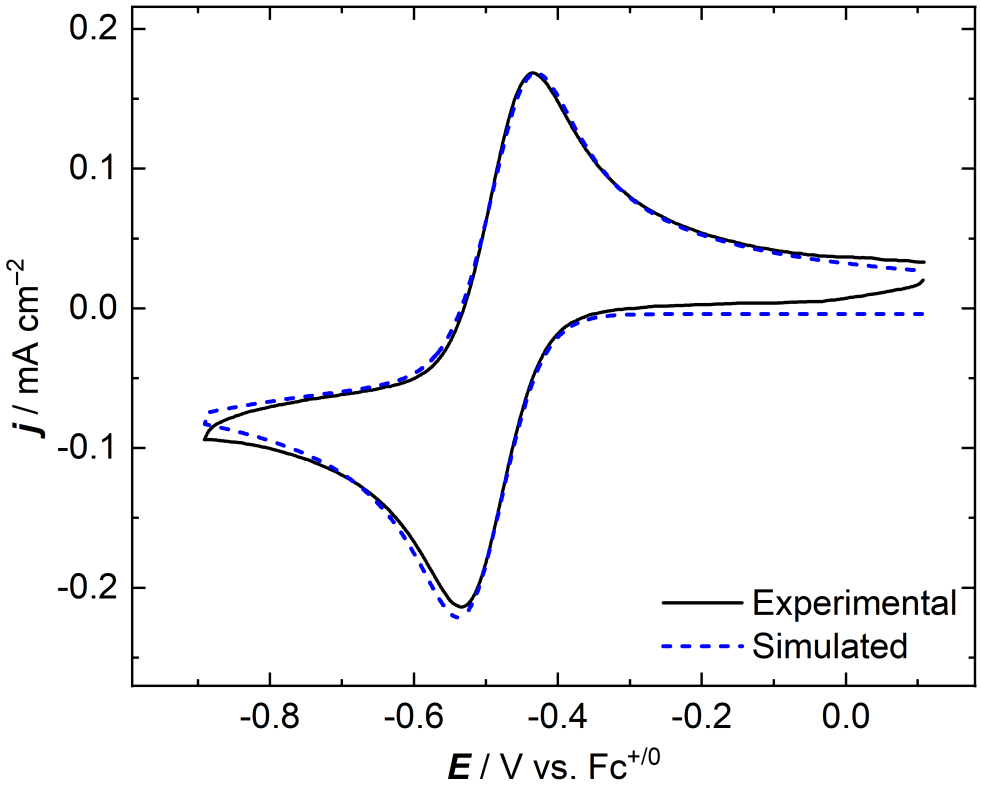

Figure S21: Experimental and simulated cyclic voltammograms of NpO_2L^{NM} in $CH_3CN/TBAPF_6$ (scan rate: 50 mV/s).

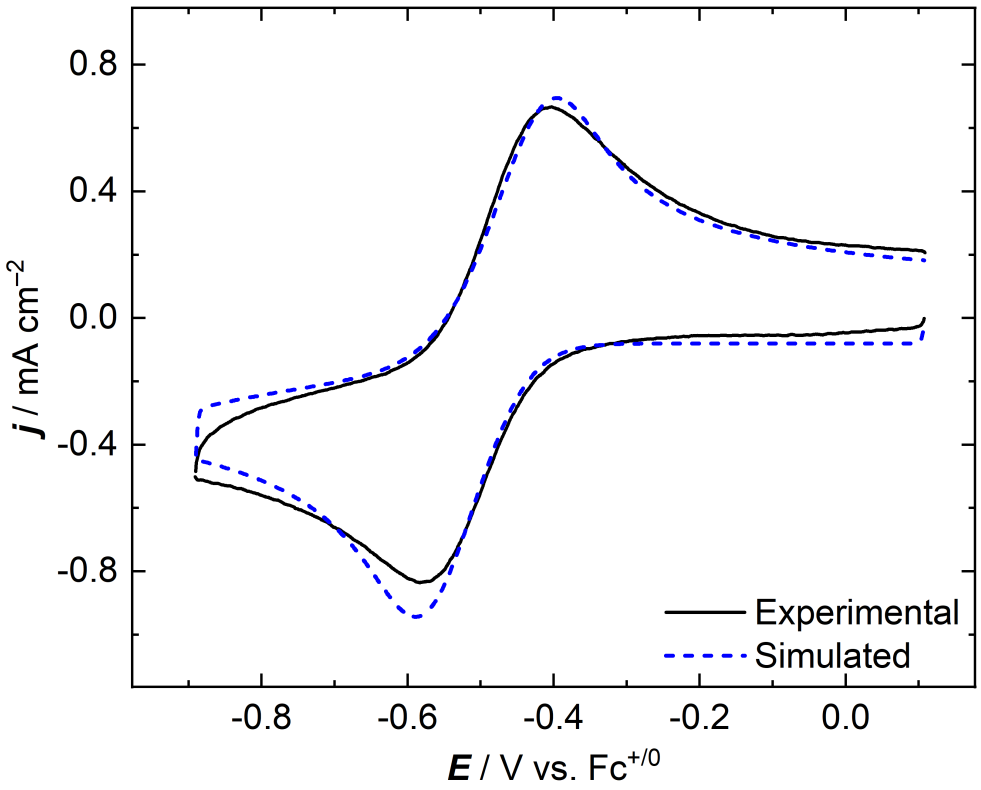

Figure S22: Experimental and simulated cyclic voltammograms of NpO_2L^{NM} in $CH_3CN/TBAPF_6$ (scan rate: 1000 mV/s).

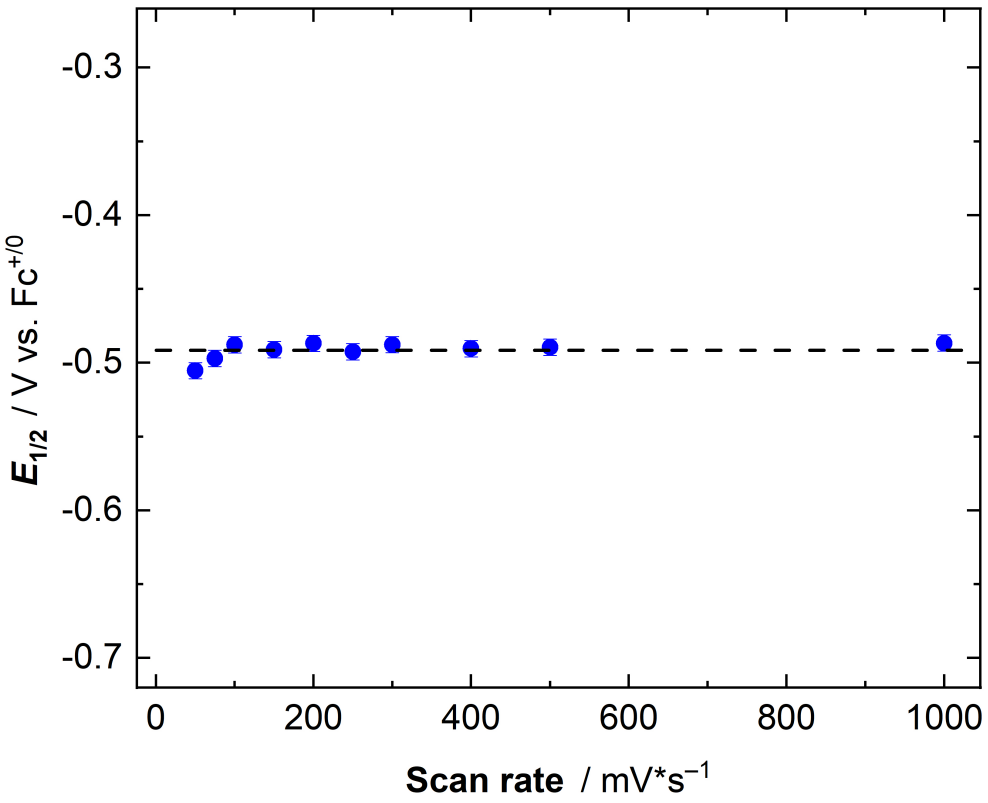

Figure S23: Sensitivity analysis of the simulated $E_{1/2}$ of NpO_2L^{NM} in CH_3CN/$TBAPF_6$ on scan rate showing no dependence. The average $E_{1/2}$ value extracted across the multiple scan rates used was –0.491 ± 0.005 V vs $Fc^{+/0}$. The $E_{1/2}$ value obtained directly from the experimental data by averaging $E_{p,a}$ and $E_{p,c}$ was –0.48 V vs $Fc^{+/0}$. Error bars shown for $E_{1/2}$ values extracted from simulations were calculated as the standard deviation of the set of values across various scan rates. These are shown as $\pm 1\sigma$ and overlaid with the arithmetic mean (dashed line).

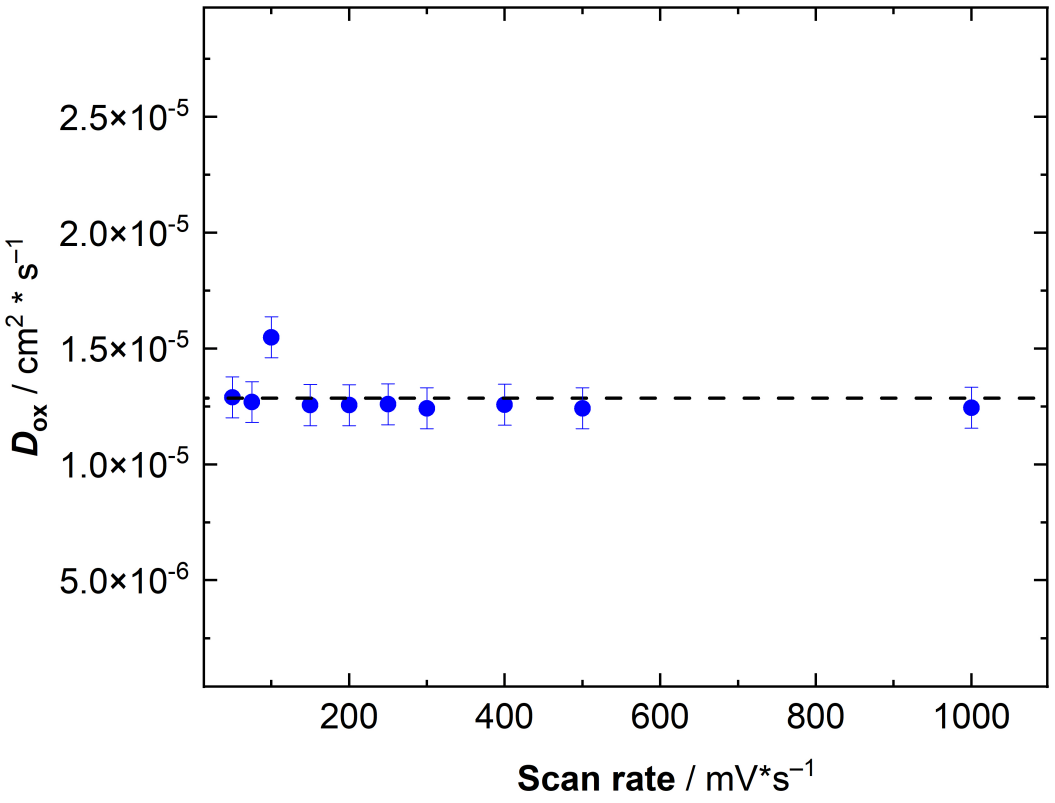

Figure S24: Sensitivity analysis of the simulated D_{ox} of NpO_2L^{NM} in CH_3CN/$TBAPF_6$ on scan rate showing no dependence. Error bars shown for D_{ox} values extracted from simulations were calculated as the standard deviation of the set of values across various scan rates. These are shown as $\pm 1\sigma$ and overlaid with the arithmetic mean (dashed line).

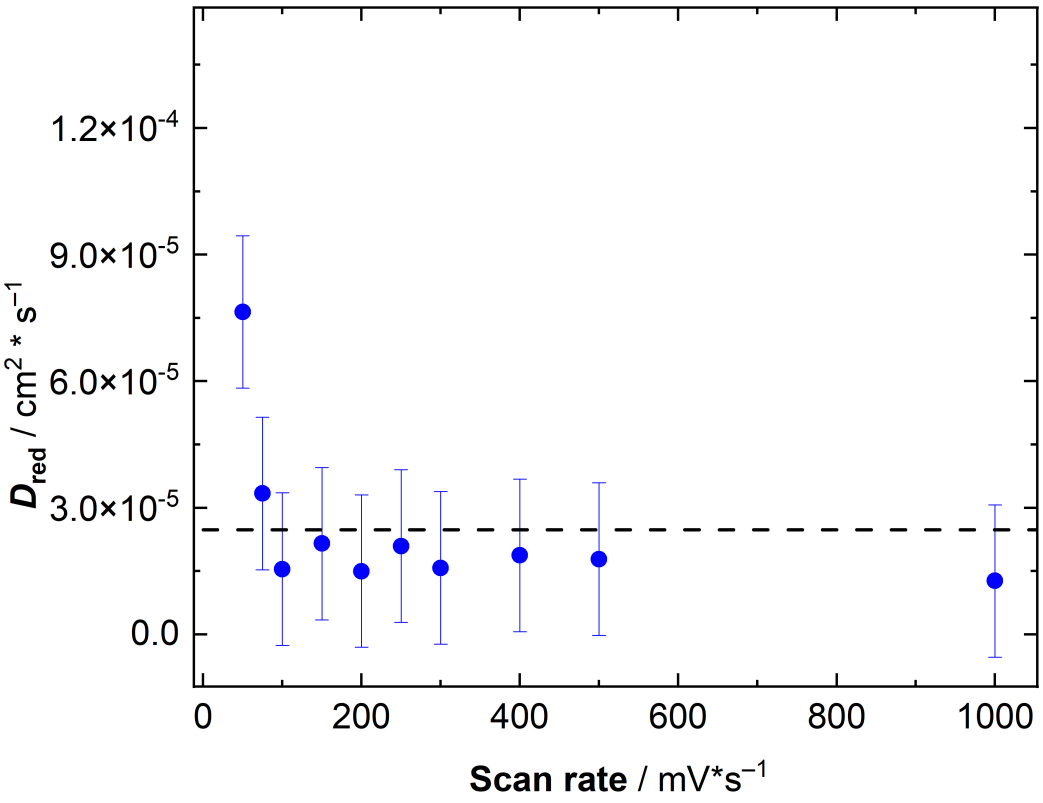

Figure S25: Sensitivity analysis of the simulated D_{red} of NpO_2L^{NM} in CH_3CN/$TBAPF_6$ on scan rate showing no dependence. Error bars shown for D_{red} values extracted from simulations were calculated as the standard deviation of the set of values across various scan rates. These are shown as $\pm 1\sigma$ and overlaid with the arithmetic mean (dashed line).

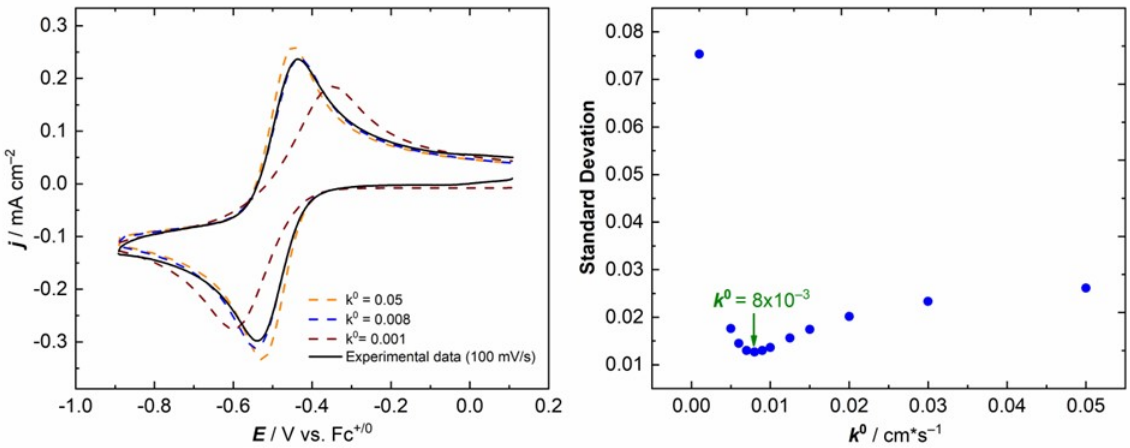

Figure S26: Evaluation of k^0 for NpO_2L^{NM} in $CH_3CN/TBAPF_6$. Left panel: Simulations with varied k^0, floated $E_{1/2}$, and fixed D_{ox}/D_{red}. Right panel: Standard deviation of $E_{1/2}$ with varied k^0, showing the optimized value of $k^0 = 0.008$ cm s^{-1}. In this context, standard deviation values are generated by the DigiElch software and indicate the goodness-of-fit of the simulated electrochemical curve to the experimental data. This was calculated from erroneous current values associated with sixteen fixed grid points along the electrochemical simulation curve following least-squares regression fitting to the experimental data.

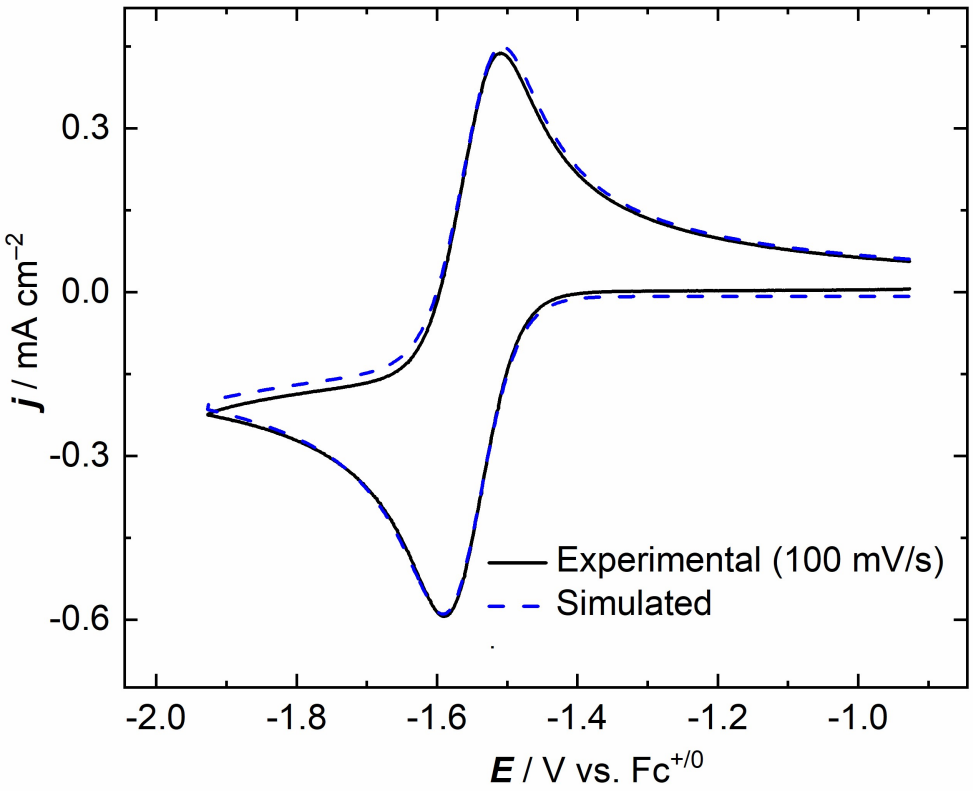

Figure S27: Experimental and simulated cyclic voltammograms of UO_2L^{NM} in $CH_3CN/TBAPF_6$ (scan rate: 100 mV/s).

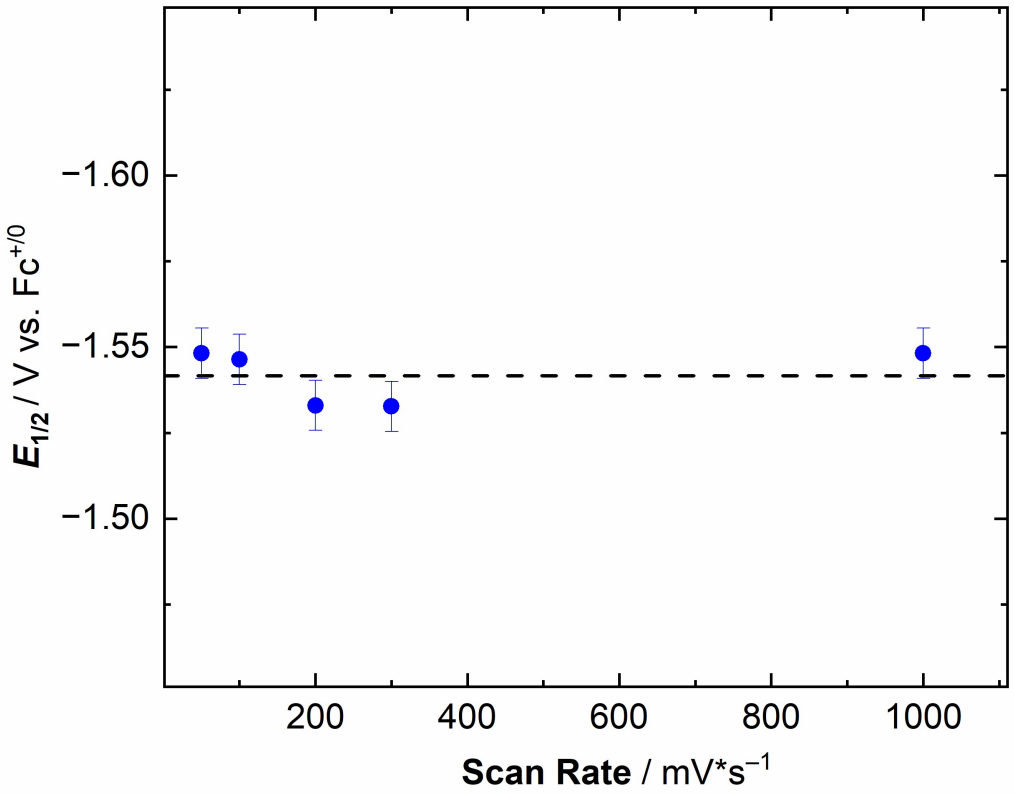

Figure S28: Sensitivity analysis of the simulated $E_{1/2}$ of UO_2L^{NM} in CH_3CN/$TBAPF_6$ on scan rate showing no dependence. Error bars shown for $E_{1/2}$ values extracted from simulations were calculated as the standard deviation of the set of values across various scan rates. These are shown as $\pm 1\sigma$ and overlaid with the arithmetic mean (dashed line).

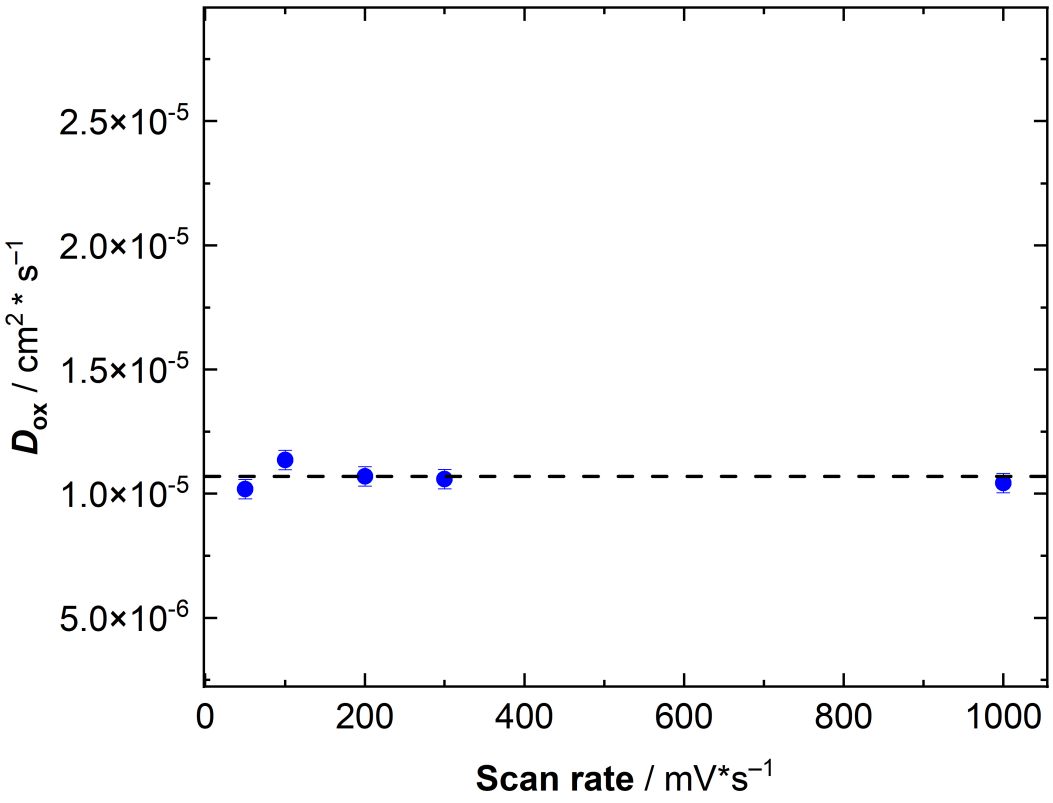

Figure S29: Sensitivity analysis of the simulated D_{ox} of UO_2L^{NM} in CH_3CN/$TBAPF_6$ on scan rate showing no dependence. Error bars shown for D_{ox} values extracted from simulations were calculated as the standard deviation of the set of values across various scan rates. These are shown as $\pm 1\sigma$ and overlaid with the arithmetic mean (dashed line).

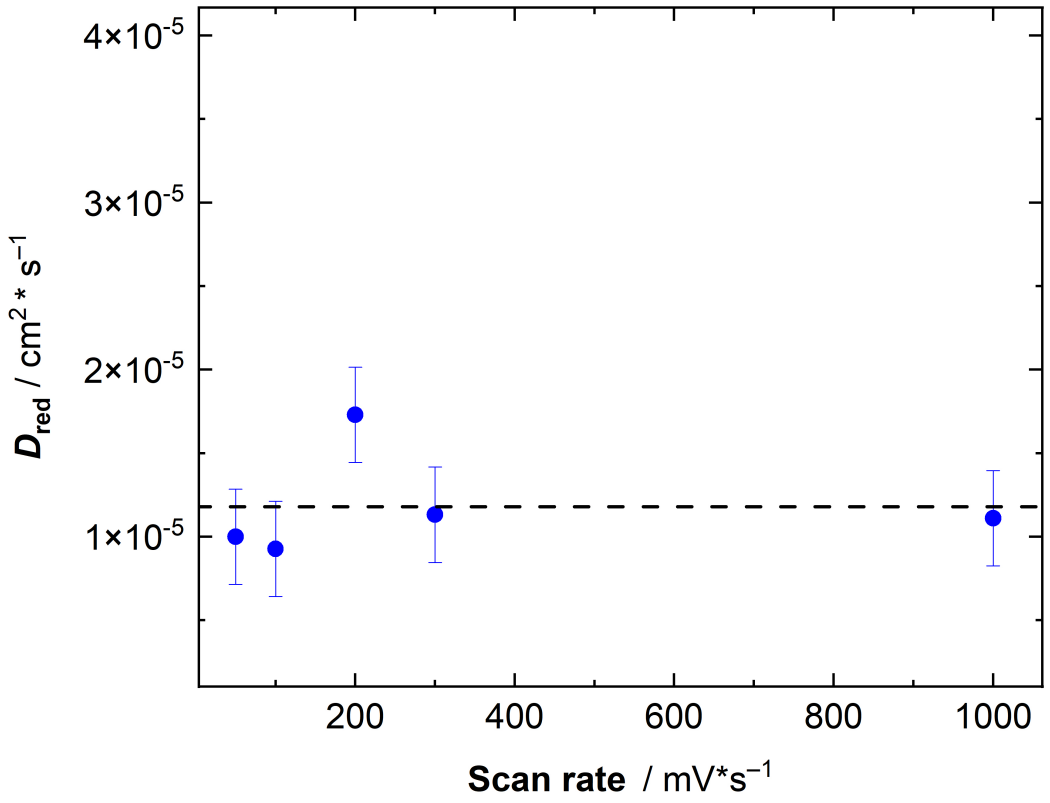

Figure S30: Sensitivity analysis of the simulated D_{red} of UO_2L^{NM} in CH_3CN/$TBAPF_6$ on scan rate showing no dependence. Error bars shown for D_{red} values extracted from simulations were calculated as the standard deviation of the set of values across various scan rates. These are shown as $\pm 1\sigma$ and overlaid with the arithmetic mean (dashed line).

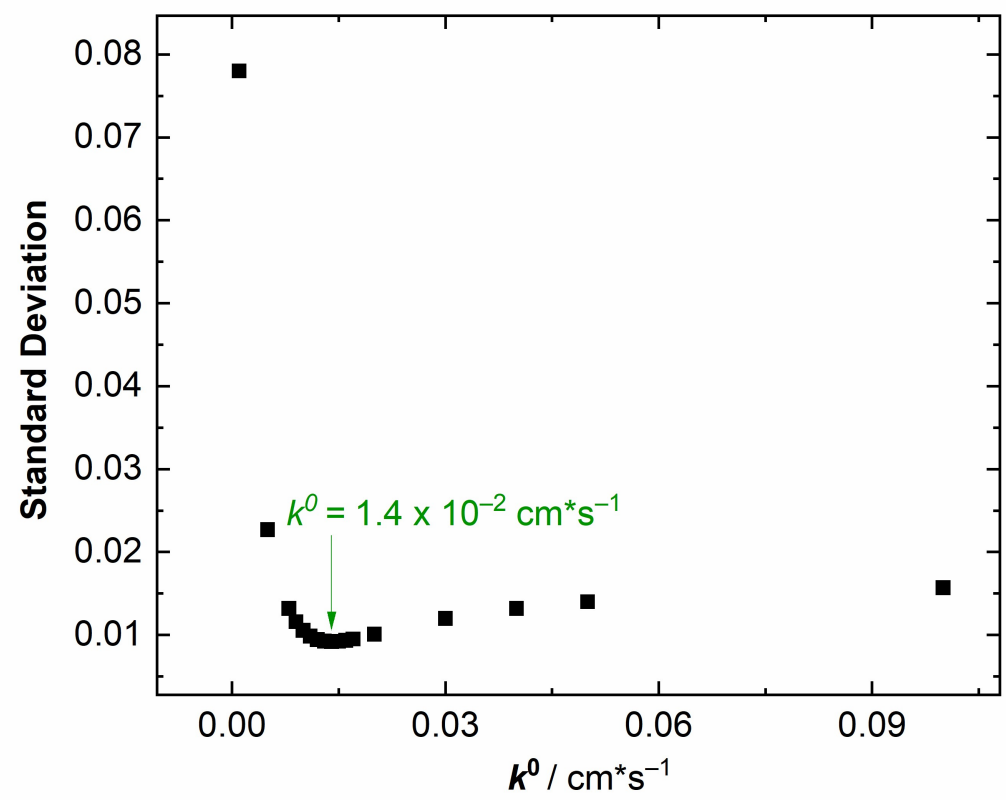

Figure S31: Evaluation of k^0 for UO_2L^{NM} in $CH_3CN/TBAPF_6$. Standard deviation of $E_{1/2}$ with varied k^0, showing the optimized value of $k^0 = 0.014$ cm s^{-1}. Standard deviation values are generated by the DigiElch software and indicate the goodness-of-fit of the simulated electrochemical curve to the experimental data. This was calculated from erroneous current values associated with sixteen fixed grid points along the electrochemical simulation curve following least-squares regression fitting to the experimental data.

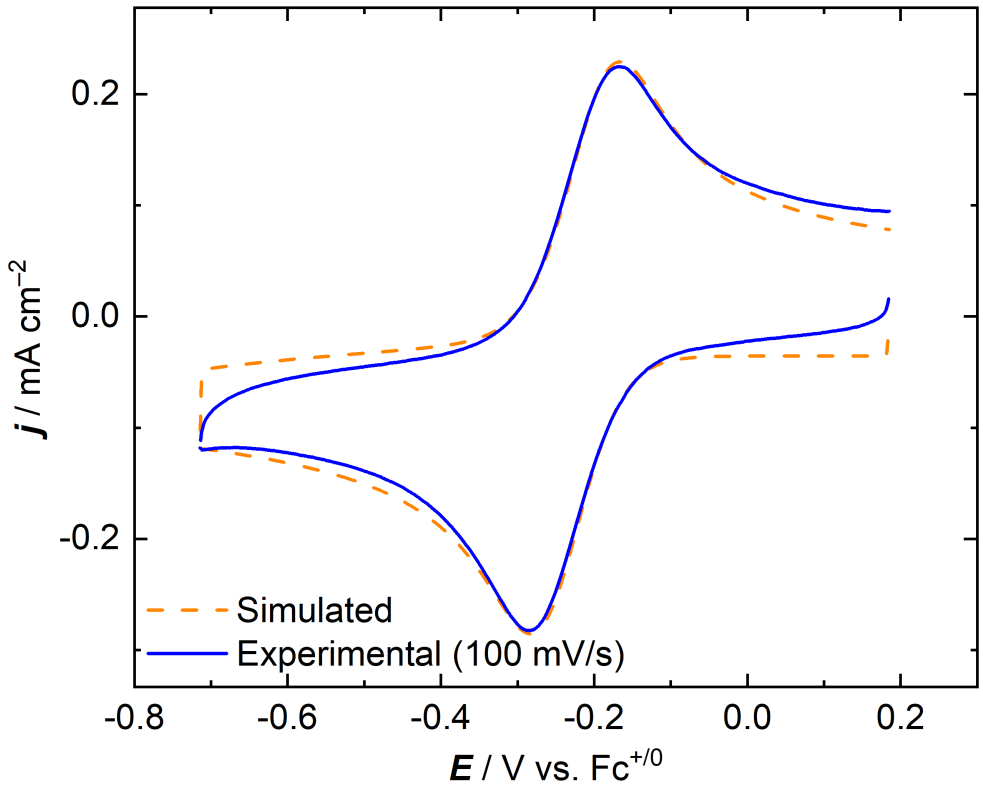

Figure S32: Experimental and simulated cyclic voltammograms of NpO_2L^{NM} in $CH_3OH/TBAPF_6$ (scan rate: 100 mV/s).

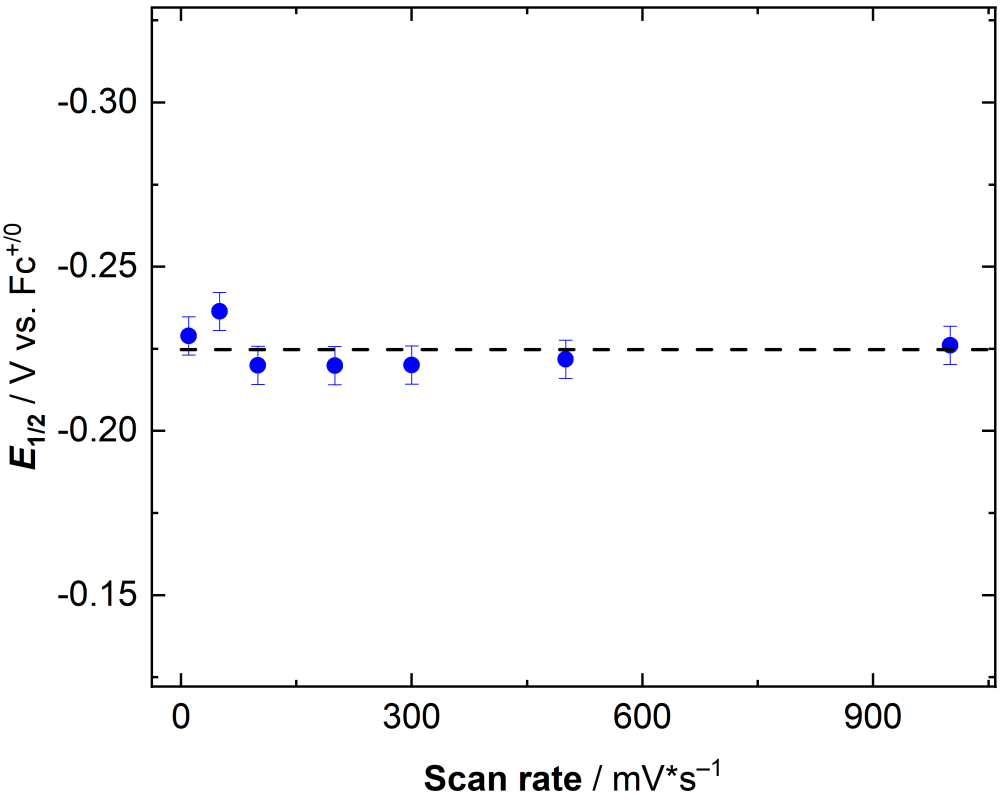

Figure S33: Sensitivity analysis of the simulated $E_{1/2}$ of NpO_2L^{NM} in CH_3OH/$TBAPF_6$ on scan rate showing no dependence. Error bars shown for $E_{1/2}$ values extracted from simulations were calculated as the standard deviation of the set of values across various scan rates. These are shown as $\pm 1\sigma$ and overlaid with the arithmetic mean (dashed line).

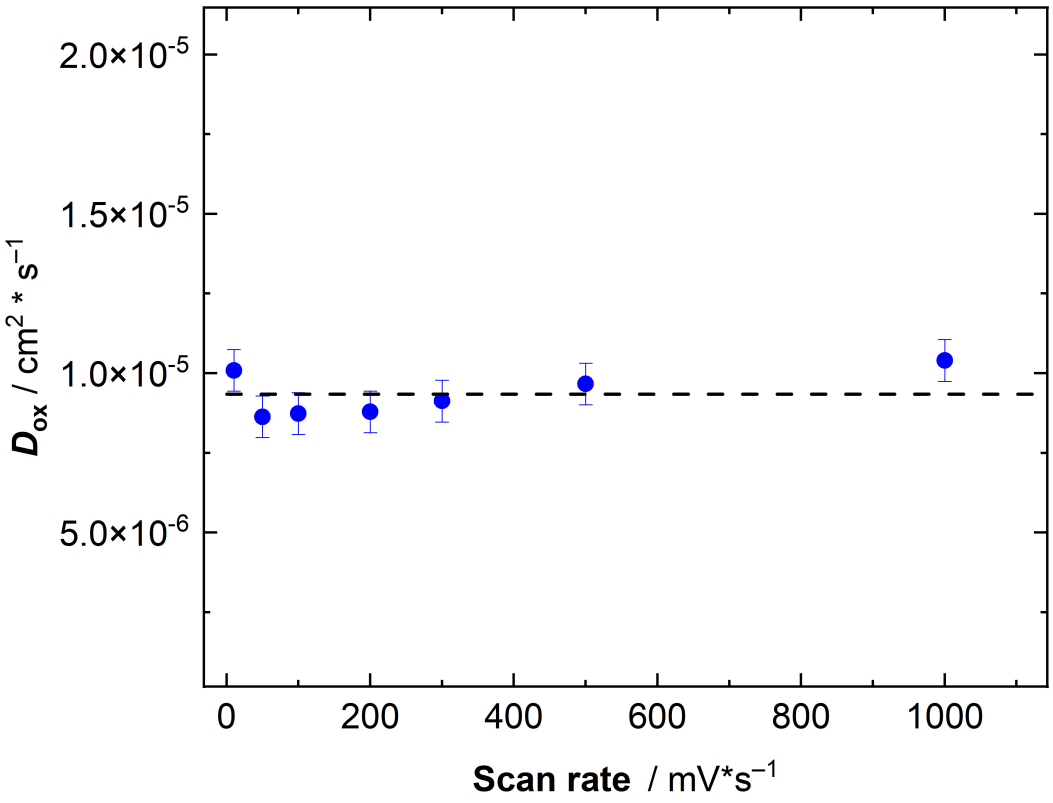

Figure S34: Sensitivity analysis of the simulated D_{ox} of NpO_2L^{NM} in $CH_3OH/TBAPF_6$ on scan rate showing no dependence.Error bars shown for D_{ox} values extracted from simulations were calculated as the standard deviation of the set of values across various scan rates. These are shown as $\pm 1\sigma$ and overlaid with the arithmetic mean (dashed line).

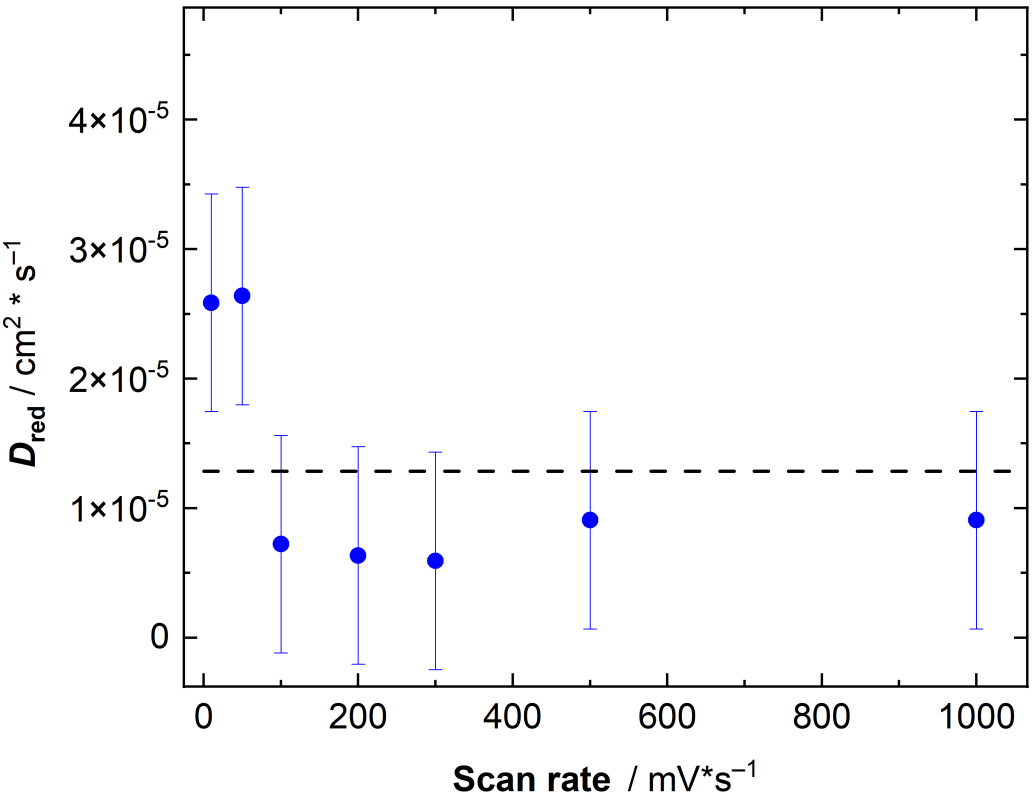

Figure S35: Sensitivity analysis of the simulated D_{red} of NpO_2L^{NM} in $CH_3OH/TBAPF_6$ on scan rate showing no dependence. Error bars shown for D_{red} values extracted from simulations were calculated as the standard deviation of the set of values across various scan rates. These are shown as $\pm 1\sigma$ and overlaid with the arithmetic mean (dashed line).

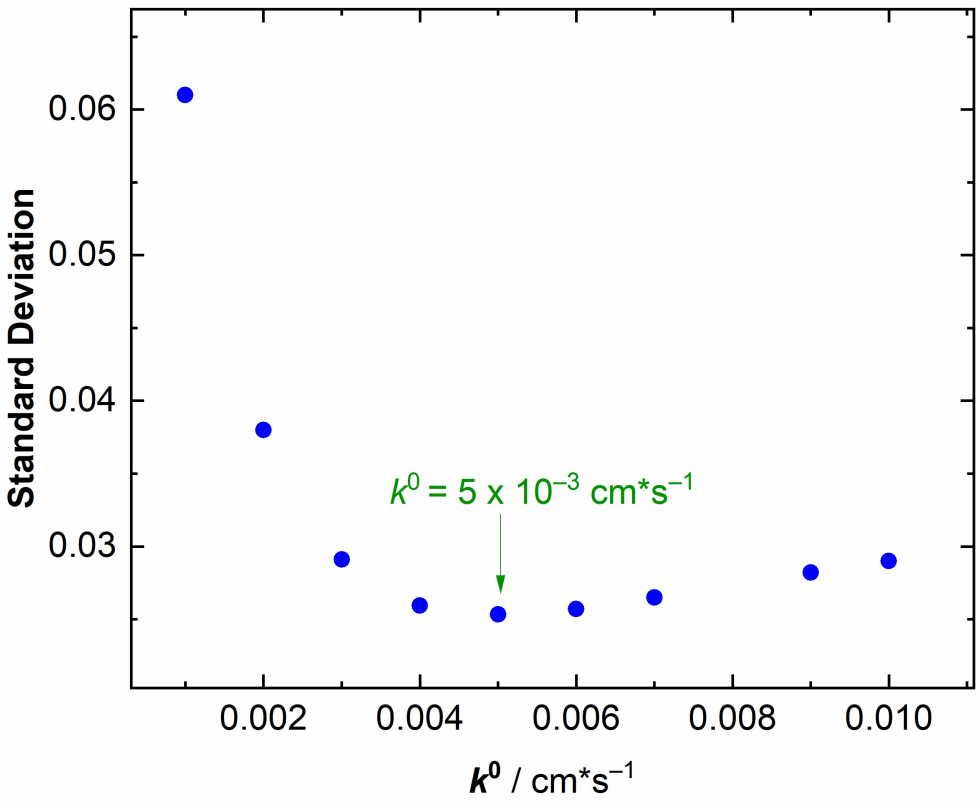

Figure S36: Evaluation of k^0 for NpO_2L^{NM} in CH_3OH/$TBAPF_6$. Standard deviation of $E_{1/2}$ with varied k^0, showing the optimized value of $k^0 = 0.005$ cm s^{-1}. Standard deviation values are generated by the DigiElch software and indicate the goodness-of-fit of the simulated electrochemical curve to the experimental data. This was calculated from erroneous current values associated with sixteen fixed grid points along the electrochemical simulation curve following least-squares regression fitting to the experimental data.

3 Spectroelectrochemistry, Spectrochemical Titration, and Electronic Absorption Spectra

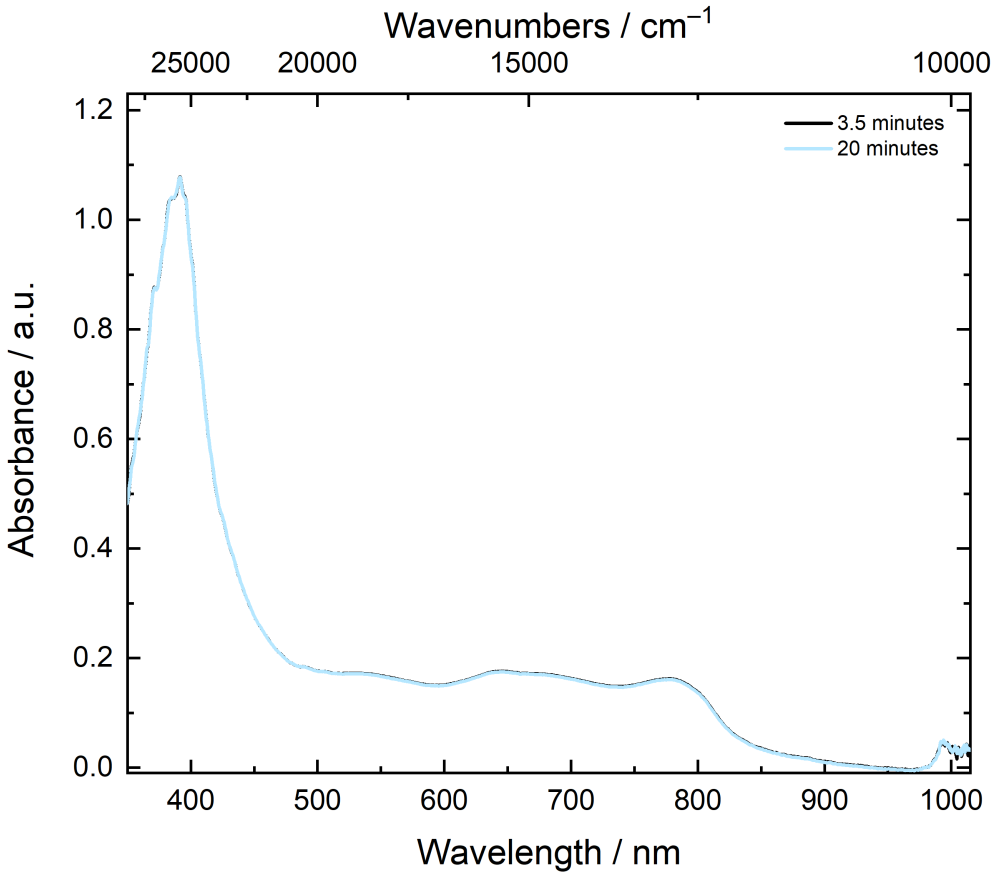

Figure S37: UV-vis spectrum of $\mathbf{NpO_2L}^{NM}$ with 1.0 equiv. Cp^*_2Fe in CH_3CN ([Np] = 0.45 mM) after 3.5 minutes of stirring vs 20 minutes of stirring, demonstrating the persistence of the Np(V) species in solution.

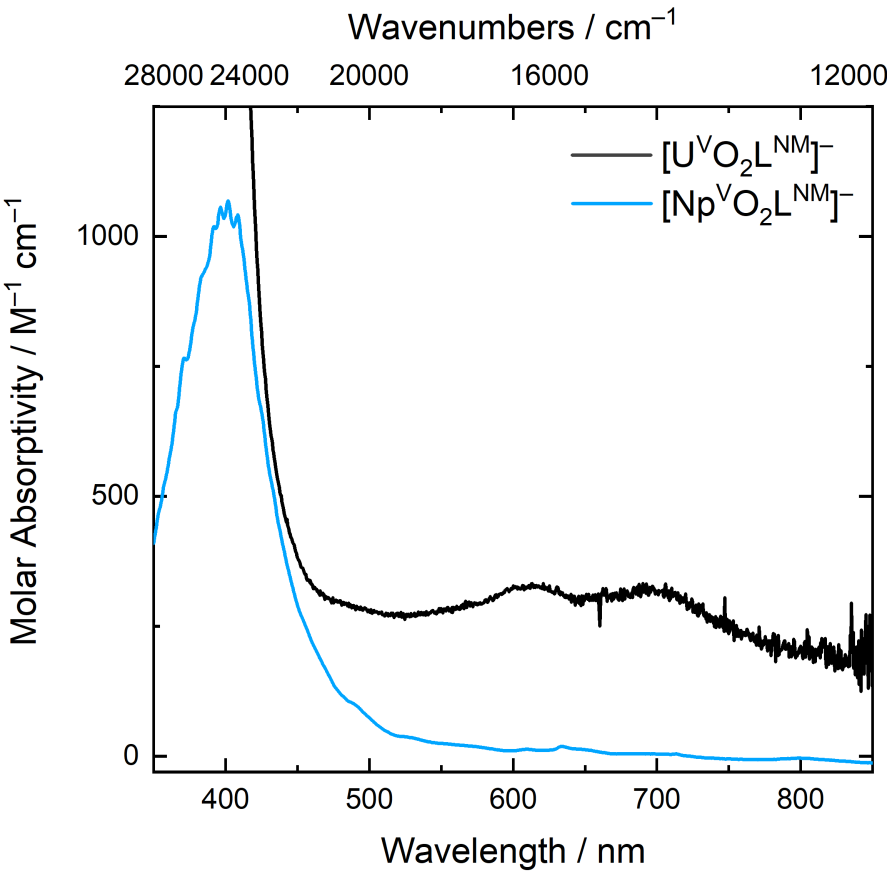

Figure S38: UV-Vis spectra of $\mathbf{[UO_2L^{NM}]^-}$ compared to in CH_3CN $\mathbf{[NpO_2L^{NM}]^-}$ in 0.2 $TBAPF_6$ in CH_3CN, highlighting the broad absorption between 500 - 800 nm in $\mathbf{[UO_2L^{NM}]^-}$ which is likely derived from a minor admixture of reduced ligand character in the formally uranium(V) species.[2] The spectrum of $\mathbf{[NpO_2L^{NM}]^-}$ does not display this feature.

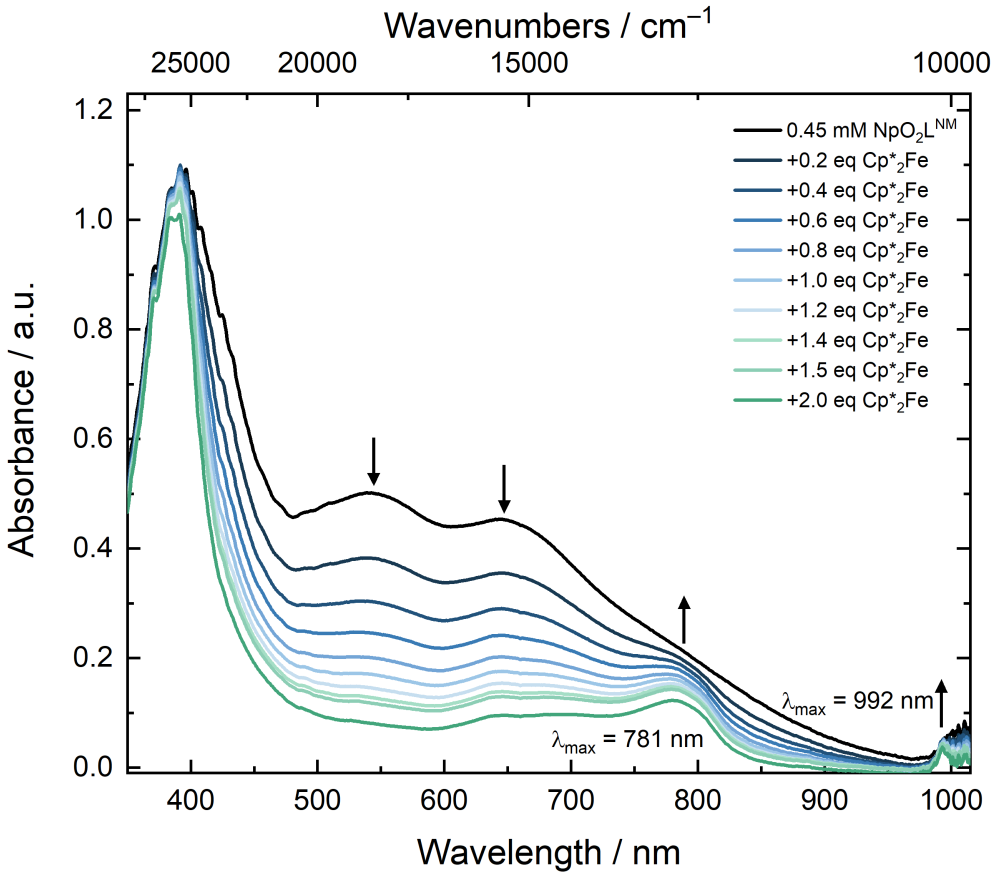

Figure S39: Spectrochemical titration of $\mathbf{NpO_2L}^{NM}$ with Cp^*_2Fe in CH_3CN ([Np] = 0.45 mM) up to 2 equiv., showing minimal changes in the Fe(III) and Np(V) spectral features.

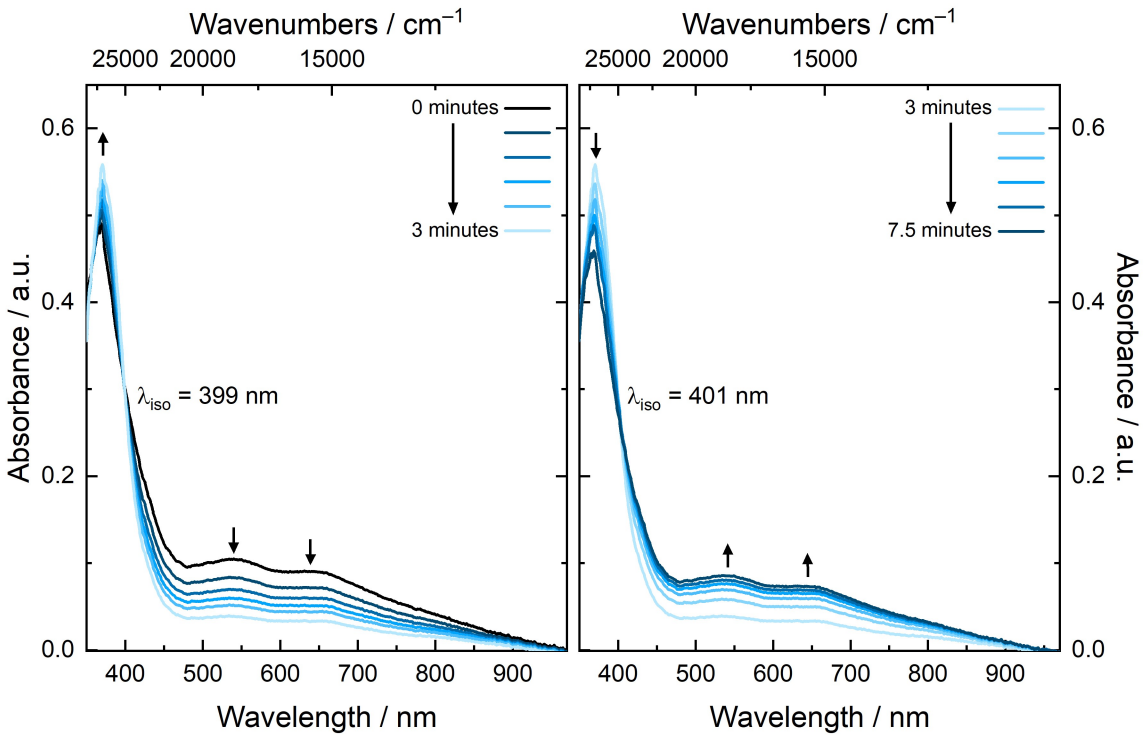

Figure S40: Spectroelectrochemical data for the electrolysis of $\mathbf{NpO_2L}^{NM}$ in CH_3OH/$TBAPF_6$. Left: polarization at -0.6 V vs $Fc^{+/0}$. Right: polarization at 0.3 V vs $Fc^{+/0}$.

4 Raman Spectra

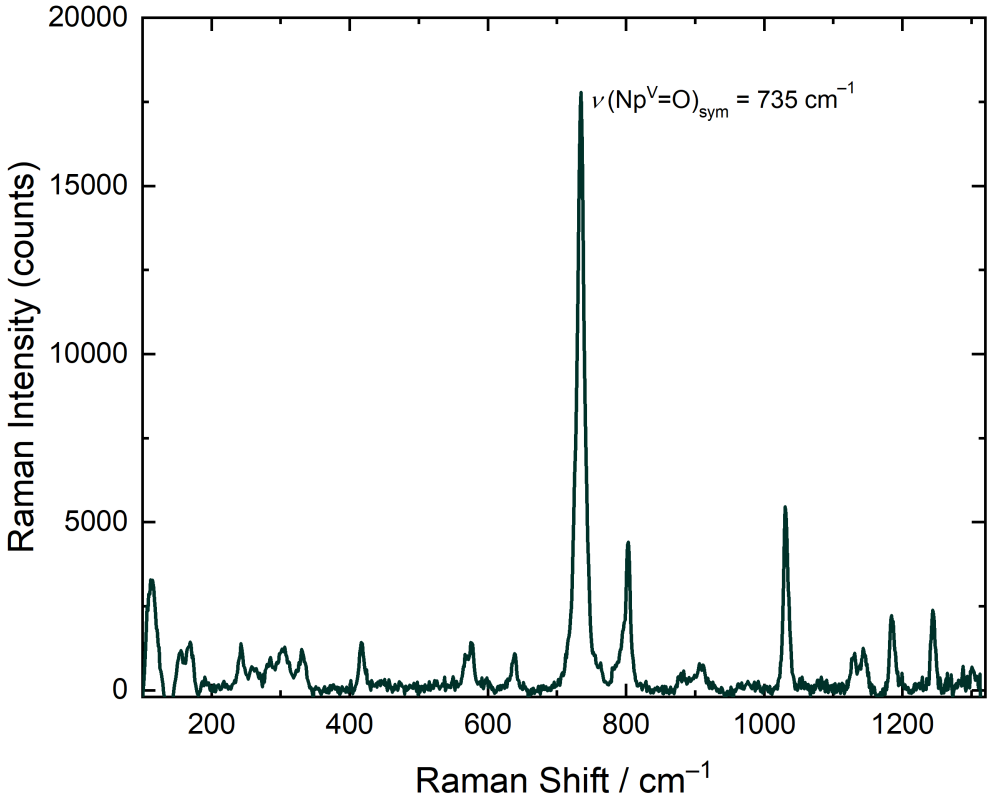

Figure S41: Solid state Raman spectrum of $\mathbf{[NpO_2L^{NM}]^- \cdot 3\,H_2O}$.

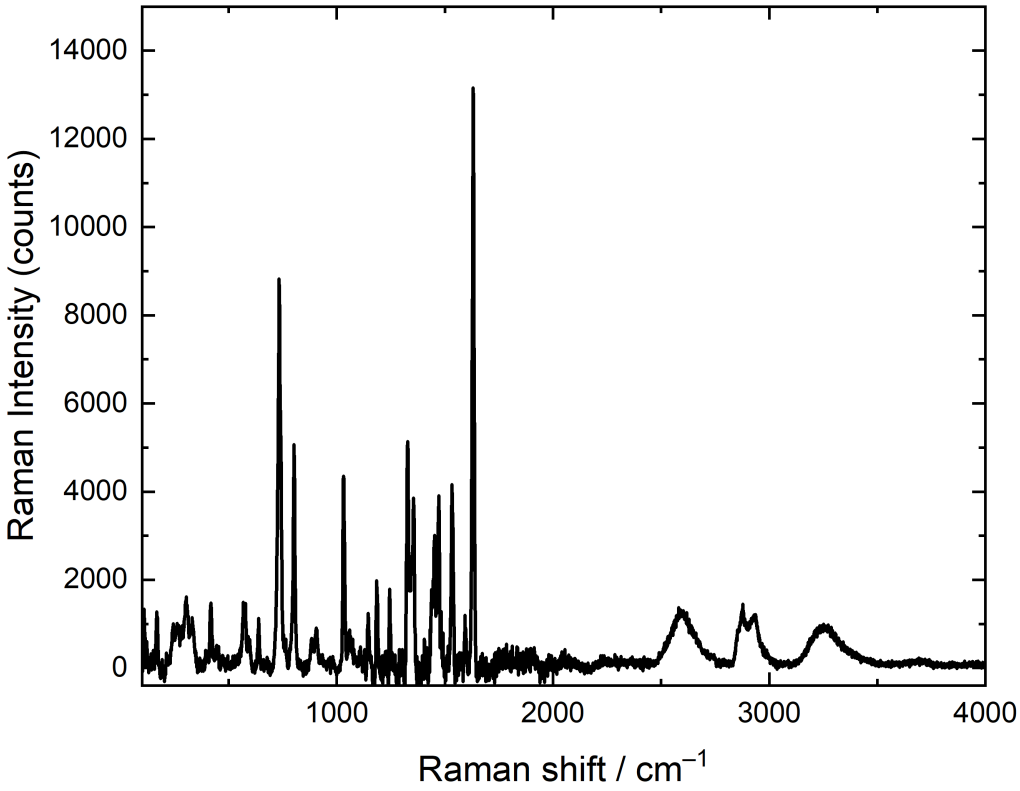

Figure S42: Full solid state Raman spectrum of $\mathbf{[NpO_2L^{NM}]^- \cdot 3\,H_2O}$.

Table S1: Assignment of selected Raman frequencies (cm^{-1}) for $\mathbf{[NpO_2L^{NM}]^- \cdot 3\,H_2O}$ and $\mathbf{[NpO_2L^{NM}]^- \cdot 2.5\,H_2O}$.

	$\mathbf{[NpO_2L^{NM}]^- \cdot 3\,H_2O}$	$\mathbf{[NpO_2L^{NM}]^- \cdot 2.5\,H_2O}$
ν(M-O_{eq})	419	418
$\nu(AnO_2)_{sym}$	735	732
ν(C-O)	803	802
$\nu(C\text{-}C)_{aromatic}$	1032	1030
$\nu(C\text{-}C)_{aromatic}$	1534	1537
ν(N=C)	1631	1631
ν(C-H)	2835 - 3000	2820 - 3000
$\nu(O\text{-}H)_{water}$	3130 - 3450	3140 - 3450

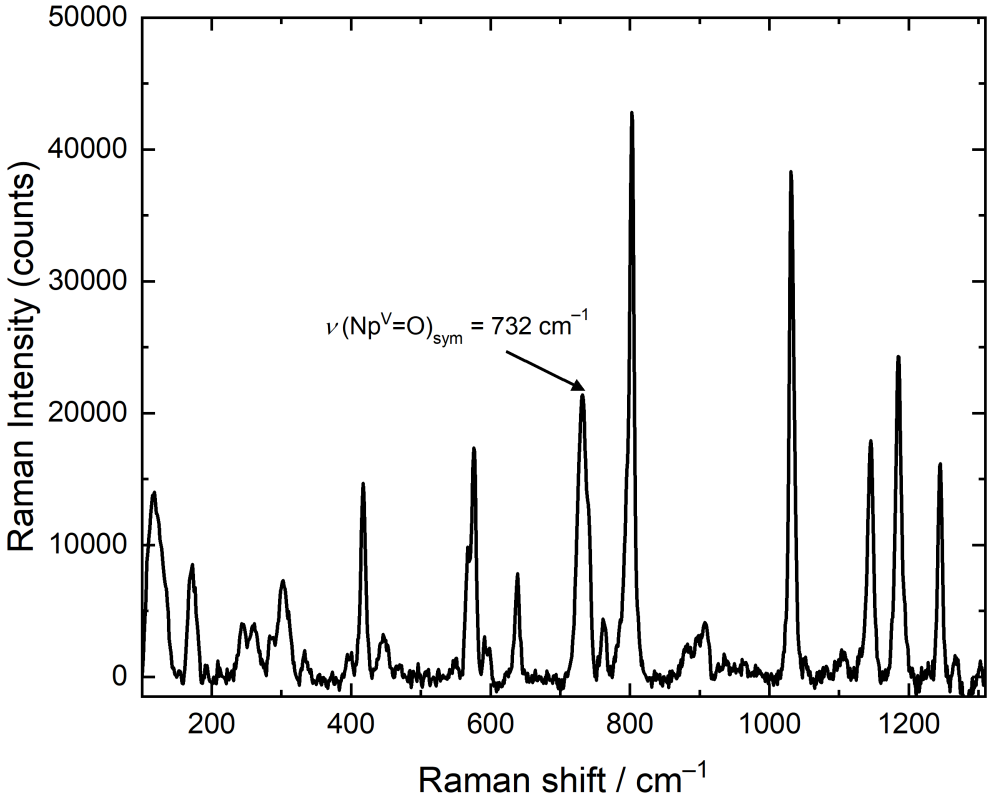

Figure S43: Solid state Raman spectrum of $\mathbf{[NpO_2L^{\mathit{NM}}]^-\cdot 2.5\,H_2O}$.

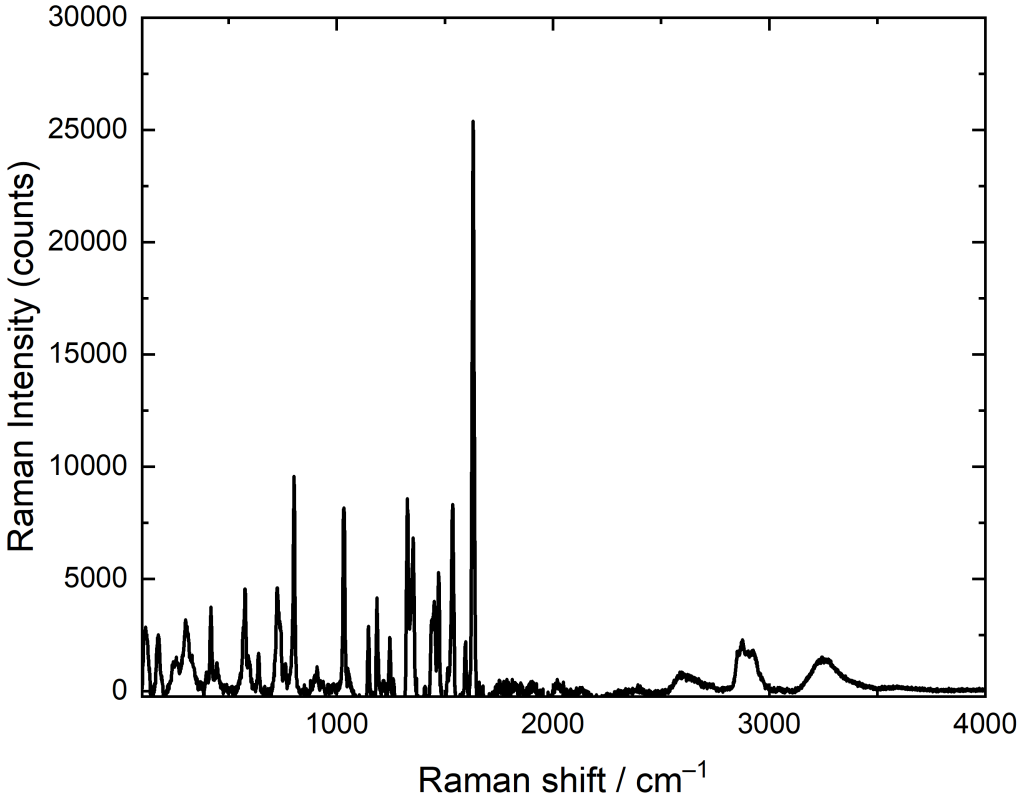

Figure S44: Full solid state Raman spectrum of $\mathbf{[NpO_2L^{\mathit{NM}}]^-\cdot 2.5\,H_2O}$.

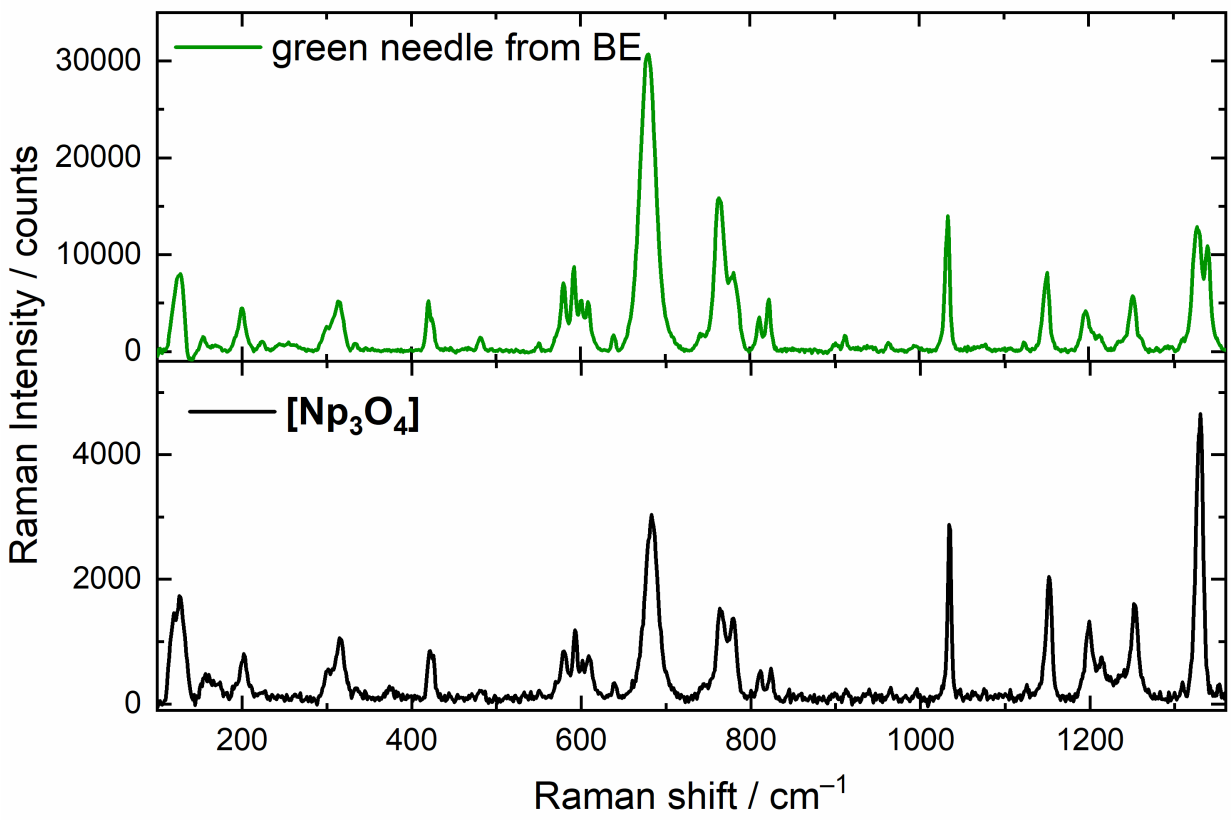

Figure S45: Comparison of Raman spectra of the green crystals produced by bulk electrolysis of NpO_2L^{NM} in MeCN electrolyte ([Np] = 0.5 mM) and **[Np_3O_4]** from a prior report.[3]

5 Crystallographic Information

5.1 Special Refinement Details for $[NpO_2L^{NM}]^- \cdot 3H_2O$ (m60a)

The structure of $[NpO_2L^{NM}]^- \cdot 3H_2O$ (m60a) crystallizes in the triclinic space group $P\bar{1}$ and the asymmetric unit contains two crystallographically independent Np sites in two molecules of $[NpO_2L^{NM}]^-$, two tetrabutylammonium counter cations, two fully occupied water molecules, and two partially-occupied water molecules. All aromatic and aliphatic protons were incorporated into the structural model as sp^3-hybridized riding model groups. Protons H4WA and H4WB were found in the difference map and fixed using AFIX 1, but the proton positions on O1W, O2W and O3W were not located and instead refined to idealized positions then fixed.

While the tetrabutylammonium cation containing N2 and C17-C32 is well-ordered, a disorder model was applied to one butyl chain in the tetrabutylammonium cation containing N1 and C1-C16. Specifically, atoms C6-C8 were modeled as being disordered over two positions in a 68/32(2) fashion (the minor orientation is denoted C6'-C8'). The bond lengths and tetrahedral bond angles for C6-C8 and C6'-C8' were restrained to appropriate multiples of the C–C bond length that was included in the refinement as a free variable which refined to a final value of 1.533(12) Å; this is reasonable considering the expected C–O bond length is 1.513 Å; the C18 - C19 distance was also restrained.[4] Finally, moderate restraints were applied to the anisotropic displacement parameters of C3, C4, C8', and C14-C19 in the form of ISOR commands.

Moderate-strength hydrogen bonding interactions can be measured between the co-crystallized water molecule O1W and molecule A with donor-acceptor distances of 2.829(7) Å for O1W···O1A and 2.805(7) Å for O1W···O2A. Additionally, O2W engages in a hydrogen bonding interaction with O4A with a donor-acceptor distance of 2.925(17) Å.[5]

Molecule B engages in similar moderate-strength hydrogen bonding interactions with

O3W and O4W with donor-acceptor distances of 2.815(8) Å for O3W···O4B, 2.972(13) Å for O4W···O1B, and 2.560(12) Å for O4W···O2B. Additionally, O4W engages in hydrogen bonding with O3W with a donor-acceptor distance of 2.710(14) Å for O3W···O4W .[5]

Finally, weak electrostatic interactions between the tetrabutylammonium cations and both molecules of $\mathbf{[NpO_2L^{NM}]^-\cdot 3H_2O}$ (m60a) throughout the structure. Donor-acceptor distances for these interactions are given in Table S2.

Table S2: Donor-acceptor distances for the weak electrostatic interactions measured in $\mathbf{[NpO_2L^{NM}]^-\cdot 3H_2O}$ (m60a).

Donor-acceptor pair	Distance (Å)
C1···O4A	3.255(10)
C14···O4A	3.332(14)
C17···O3A	3.188(10)
C25···O1W	3.282(9)
C23···O3B	3.371(9)
C21···O3B	3.075(8)
C15B···O4B	3.364(10)
C5···O1B	3.413(13)

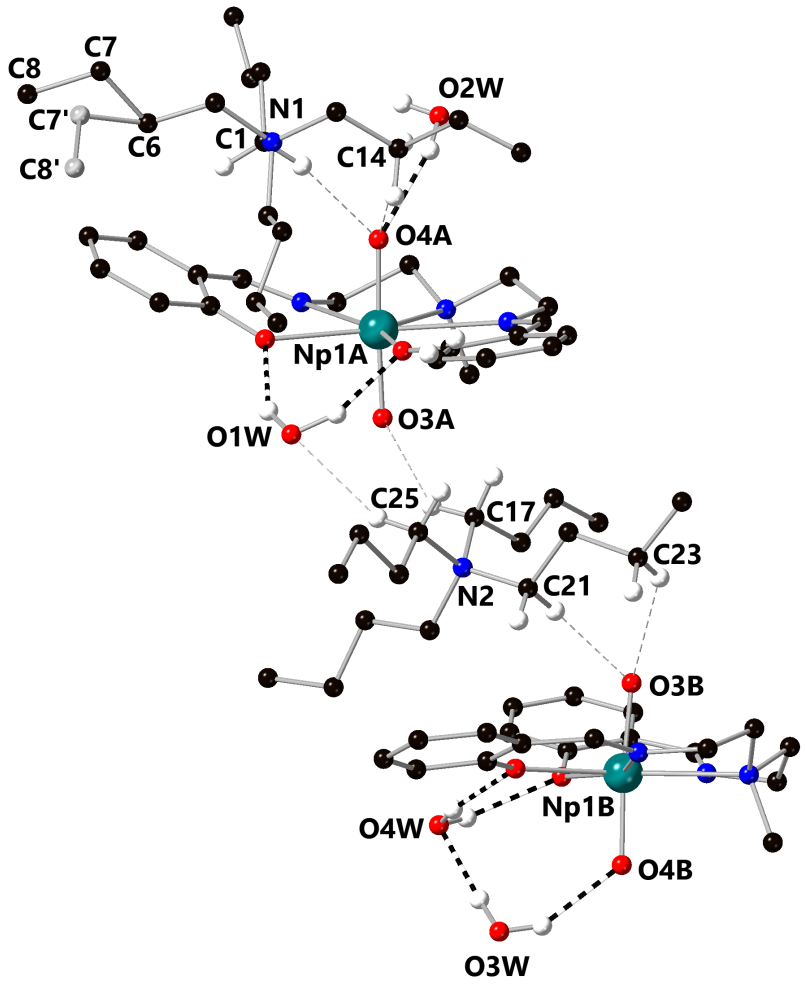

Figure S46: Ball and stick representation of the asymmetric unit of $\mathbf{[NpO_2L^{NM}]^-\cdot 3H_2O}$ (m60a). Hydrogen bonding interactions are denoted with bold dashed lines and weak electrostatic interactions with the NpO_2^+ cores are denoted with gray dashed lines. All hydrogen atoms except those engaged in the noted interactions are omitted for clarity and disordered atoms are shown in gray.

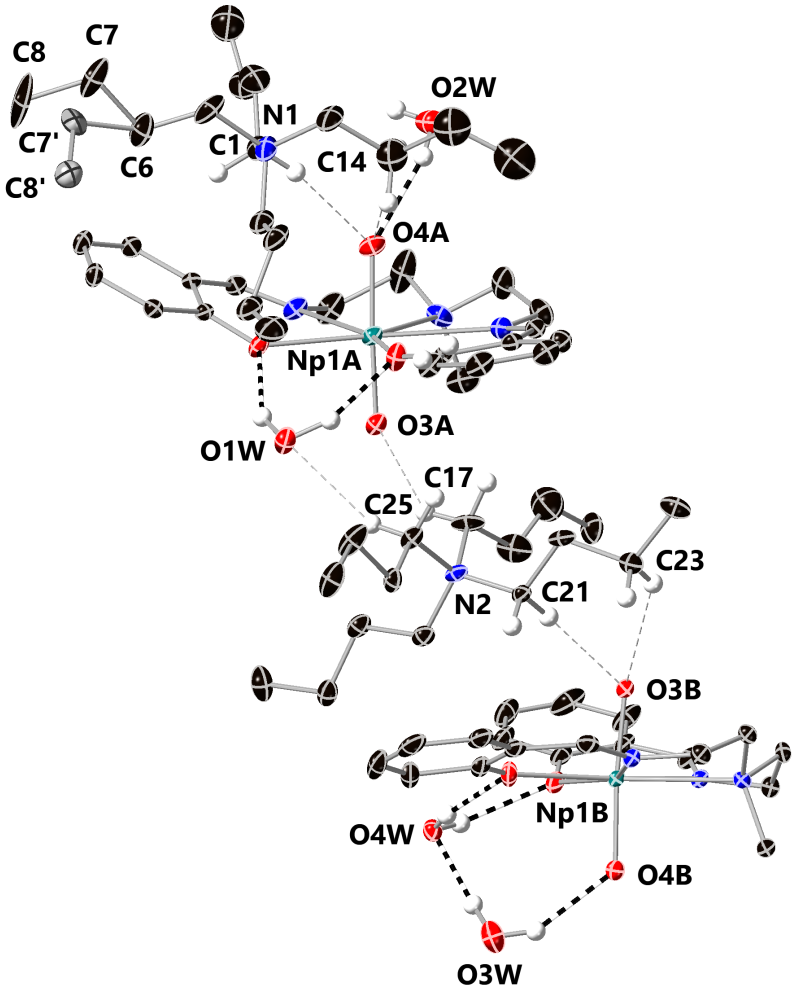

Figure S47: Asymmetric unit of $\mathbf{[NpO_2L^{NM}]^- \cdot 3H_2O}$ (m60a). Hydrogen bonding interactions are denoted with bold dashed lines and weak electrostatic interactions with the NpO_2^+ cores are denoted with gray dashed lines. All hydrogen atoms except those engaged in the noted interactions are omitted for clarity and disordered atoms are shown in gray. Displacement ellipsoids are shown at the 20% probability level.

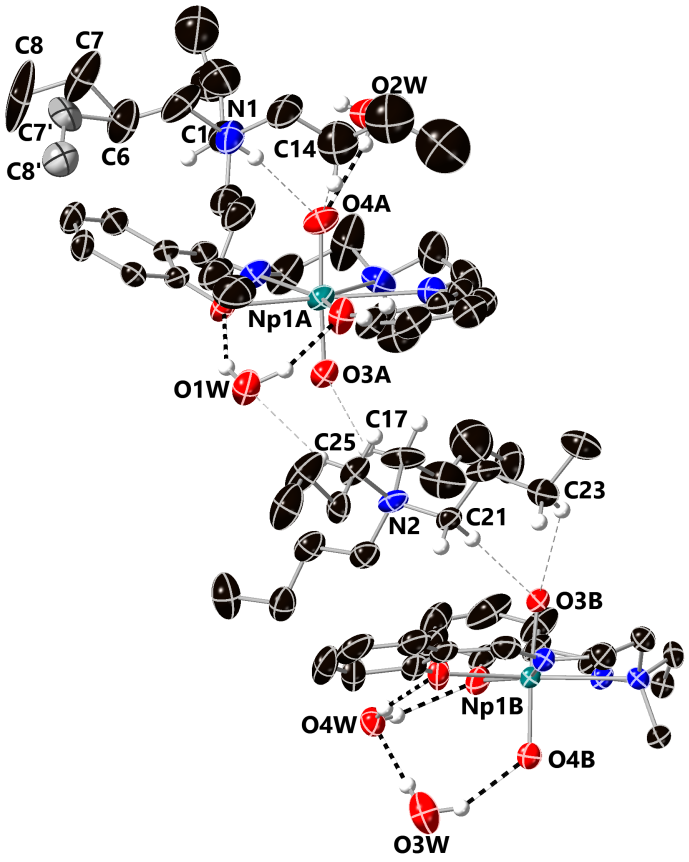

Figure S48: Asymmetric unit of $\mathbf{[NpO_2L^{NM}]^- \cdot 3H_2O}$ (m60a). Hydrogen bonding interactions are denoted with bold dashed lines and weak electrostatic interactions with the NpO_2^+ cores are denoted with gray dashed lines. All hydrogen atoms except those engaged in the noted interactions are omitted for clarity and disordered atoms are shown in gray. Displacement ellipsoids are shown at the 50% probability level.

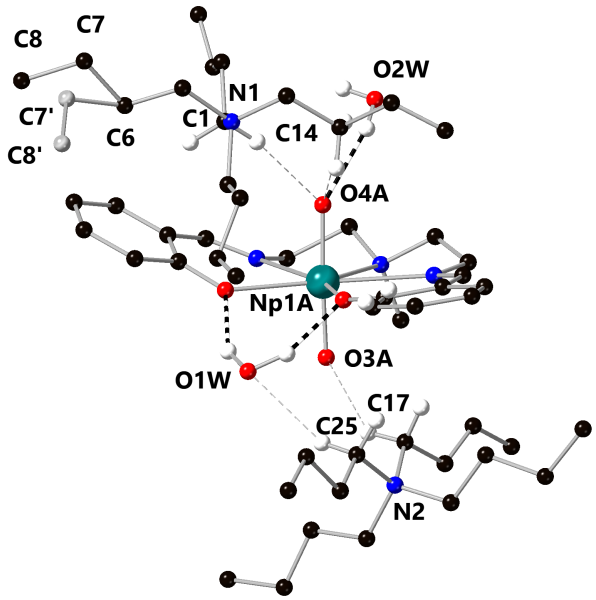

Figure S49: Molecule A of $\mathbf{[NpO_2L^{NM}]^- \cdot 3H_2O}$ (m60a) and the tetrabutylammonium ions that interact with it in the solid-state. Hydrogen bonding interactions are denoted with bold dashed lines and weak electrostatic interactions with the NpO_2^+ cores are denoted with gray dashed lines. Molecule B and all hydrogen atoms except those engaged in the noted interactions are omitted for clarity.

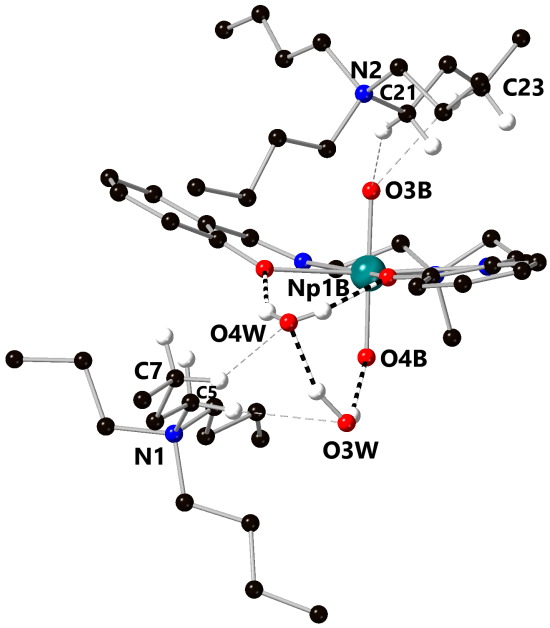

Figure S50: Molecule B of $\mathbf{[NpO_2L^{NM}]^- \cdot 3H_2O}$ (m60a) and the tetrabutylammonium ions that interact with it in the solid-state. Hydrogen bonding interactions are denoted with bold dashed lines and weak electrostatic interactions with the NpO_2^+ cores are denoted with gray dashed lines. Molecule A, disordered atoms, and all hydrogen atoms except those engaged in the noted interactions are omitted for clarity.

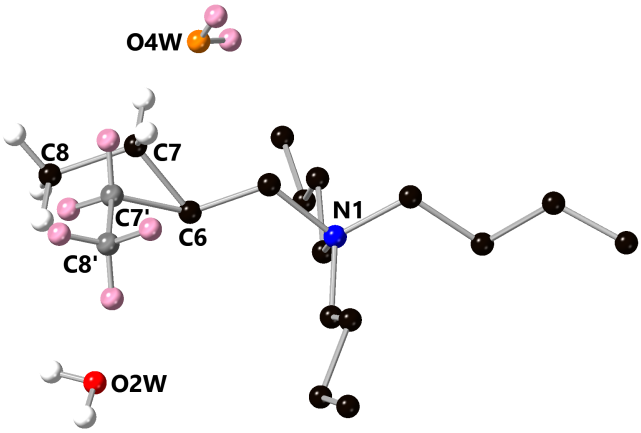

Figure S51: Disorder model of the tetrabutylammonium cation containing N1 and the two partially occupied water molecules O2W and O4W. The position of O2W is linked to the positions of C6, C7, and C8, while the position of O4W is linked to C6', C7', and C8'. The minor disorder orientation is shown in lighter atom colors. Molecules A and B, the tetrabutylammonium ion containing N2, and all other hydrogen atoms are omitted for clarity.

5.2 Special Refinement Details for $[NpO_2L^{NM}]^-\cdot 2.5H_2O$ (m36a)

The structure of $[NpO_2L^{NM}]^-\cdot 2.5H_2O$ (m36a) crystallizes in the triclinic space group $P\bar{1}$ and the asymmetric unit contains crystallographically independent Np sites in two molecules of $[NpO_2L^{NM}]^-$, two tetrabutylammonium counter cations, two fully occupied water molecules, and one half-occupied water molecule. All aromatic and aliphatic protons were incorporated into the structural model as sp^3-hybridized riding model groups. Protons positions on O1W, O2W and O3W were not located in the difference map and were refined to idealized positions then fixed.

While the tetrabutylammonium cation containing N1 and C1-C16 is well-ordered, a disorder model was applied to one butyl chain in the tetrabutylammonium cation containing N2 and C17-C32. Specifically, atoms C22-C24 were modeled as being disordered over two positions in a 57/43(1) fashion (the minor orientation is denoted C22'-C24'). The bond lengths and tetrahedral bond angles for C22-C24 and C22'-C24' were restrained to appropriate multiples of the C–C bond length that was included in the refinement as a free variable which refined to a final value of 1.555(7) Å; this is reasonable considering the expected C–O bond length is 1.513 Å.[4] Finally, moderate restraints were applied to the anisotropic displacement parameters of C14, C15, C22, C23, C24, C22', C23', C24', C27, C28, C29, C30, and C31 in the form of ISOR and SIMU commands.

Moderate-strength hydrogen bonding interactions can be measured between the co-crystallized water molecule O1W and molecule A with donor-acceptor distances of 2.837(7) Å for O1W$\cdots$O1A and 2.819(8) Å for O1W$\cdots$O2A; no hydrogen bonding interactions with the actinyl oxos of molecule A are present.[5]

Molecule B engages in similar moderate-strength hydrogen bonding interactions with O2W and O3W with donor-acceptor distances of 2.817(7) Å for O2W$\cdots$O4B, 2.530(14) Å for O3W$\cdots$O1B, and 2.962(15) Å for O3W$\cdots$O2B.[5]

Finally, weak electrostatic interactions between the tetrabutylammonium cations and

both molecules of $\mathbf{[NpO_2L^{NM}]^-\cdot 2.5H_2O}$ (m36a) throughout the structure. Donor-acceptor distances for these interactions are given in Table S3.

Table S3: Donor-acceptor distances for the weak electrostatic interactions measured in $\mathbf{[NpO_2L^{NM}]^-\cdot 2.5H_2O}$ (m36a).

Donor-acceptor pair	Distance (Å)
C25···O4A	3.256(9)
C22···O4A	3.348(11)
C1A···O3A	3.107(7)
C13···O3A	3.221(9)
C1···O3B	3.076(8)
C3···O3B	3.371(8)
C18B···O4B	3.388(8)
C21···O4B	3.585(10)

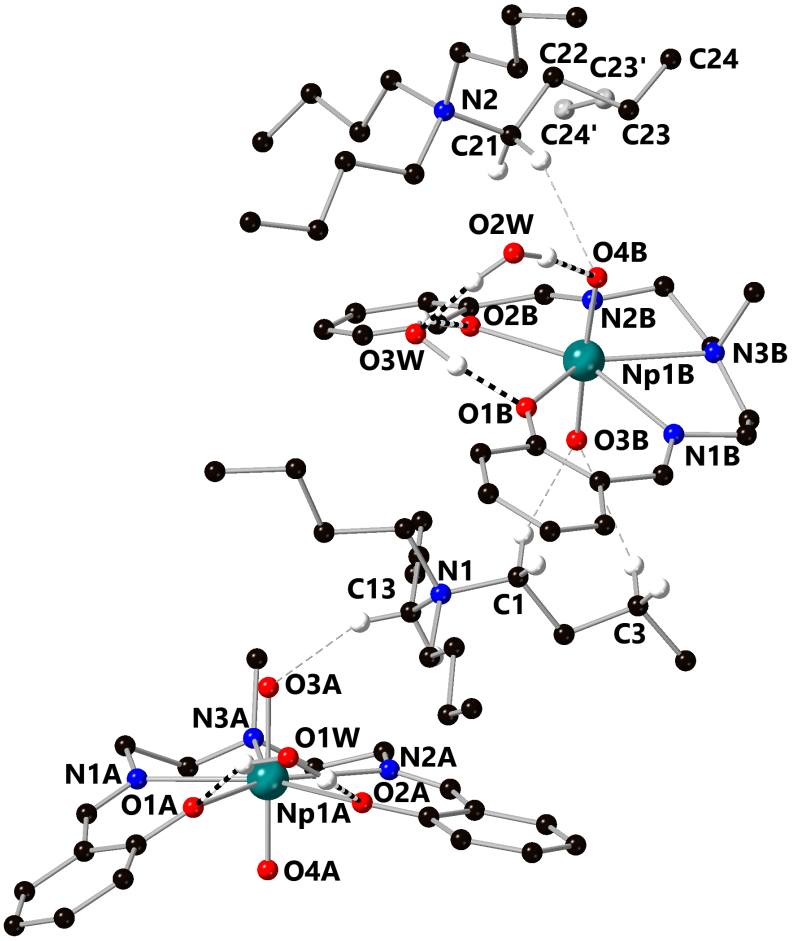

Figure S52: Ball and stick representation of the asymmetric unit of $\mathbf{[NpO_2L^{NM}]^- \cdot 2.5H_2O}$ (m36a). Hydrogen bonding interactions are denoted with bold dashed lines and weak electrostatic interactions with the NpO_2^+ cores are denoted with gray dashed lines. All hydrogen atoms except those engaged in the noted interactions are omitted for clarity and disordered atoms are shown in gray.

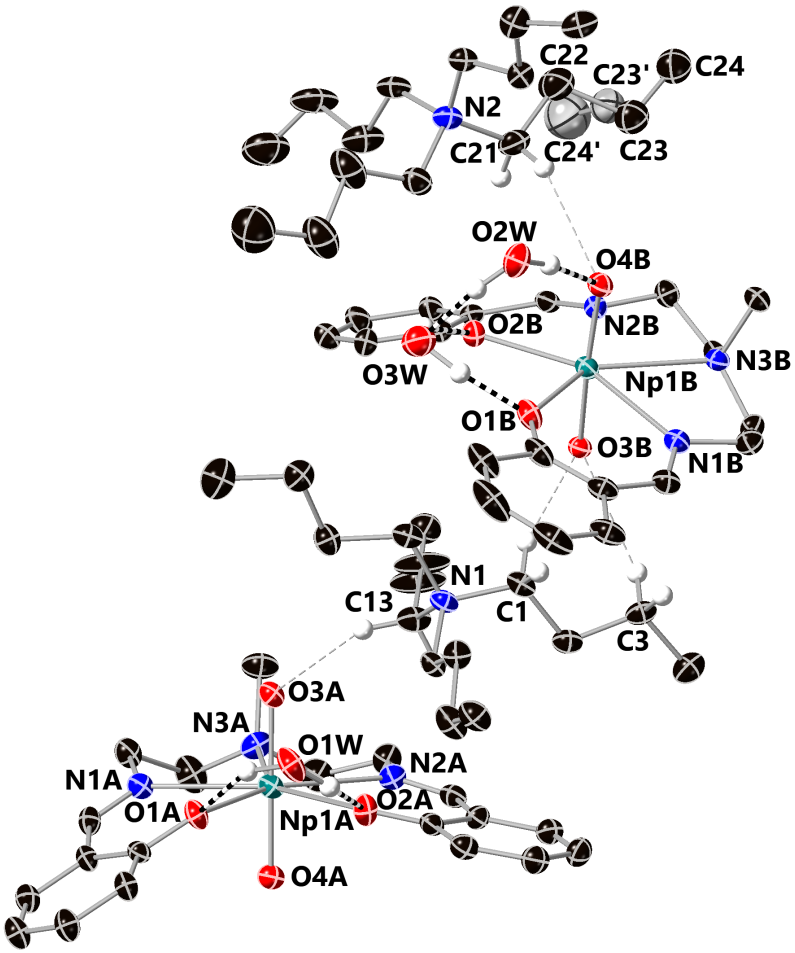

Figure S53: Asymmetric unit of $\mathbf{[NpO_2L^{NM}]^- \cdot 2.5H_2O}$ (m36a). Hydrogen bonding interactions are denoted with bold dashed lines and weak electrostatic interactions with the NpO_2^+ cores are denoted with gray dashed lines. All hydrogen atoms except those engaged in the noted interactions are omitted for clarity and disordered atoms are shown in gray. Displacement ellipsoids are shown at the 20% probability level.

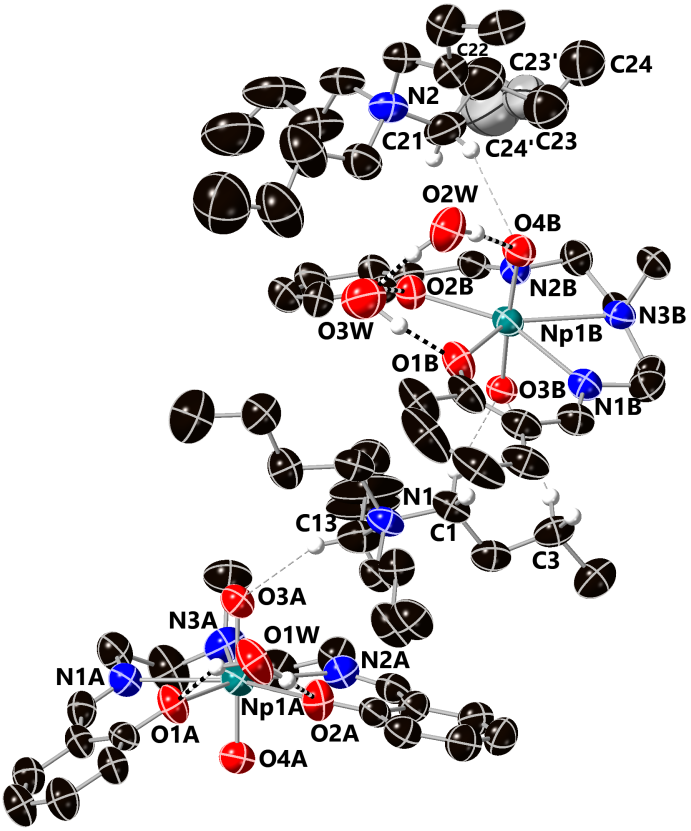

Figure S54: Asymmetric unit of $\mathbf{[NpO_2L^{NM}]^-\cdot 2.5H_2O}$ (m36a). Hydrogen bonding interactions are denoted with bold dashed lines and weak electrostatic interactions with the NpO_2^+ cores are denoted with gray dashed lines. All hydrogen atoms except those engaged in the noted interactions are omitted for clarity and disordered atoms are shown in gray. Displacement ellipsoids are shown at the 50% probability level.

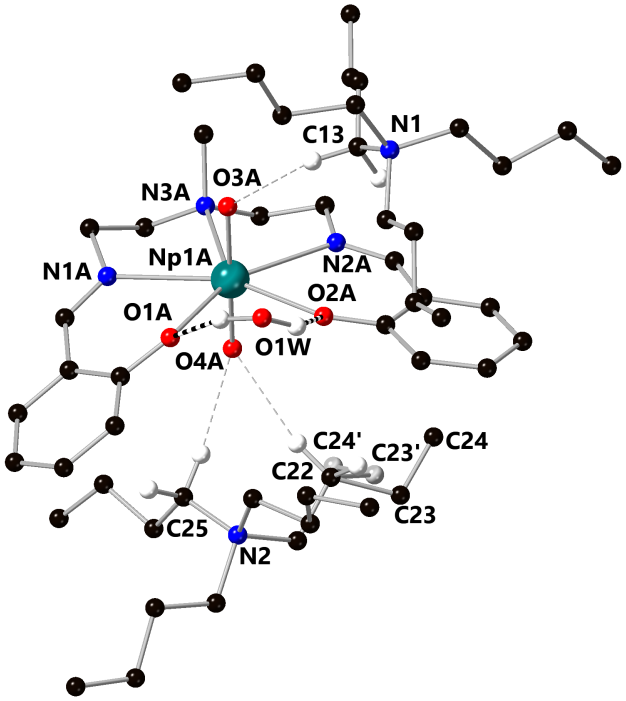

Figure S55: Molecule A of $\mathbf{[NpO_2L^{NM}]^-\cdot 2.5H_2O}$ (m36a) and the tetrabutylammonium ions that interact with it in the solid-state. Hydrogen bonding interactions are denoted with bold dashed lines and weak electrostatic interactions with the NpO_2^+ cores are denoted with gray dashed lines. Molecule B and all hydrogen atoms except those engaged in the noted interactions are omitted for clarity.

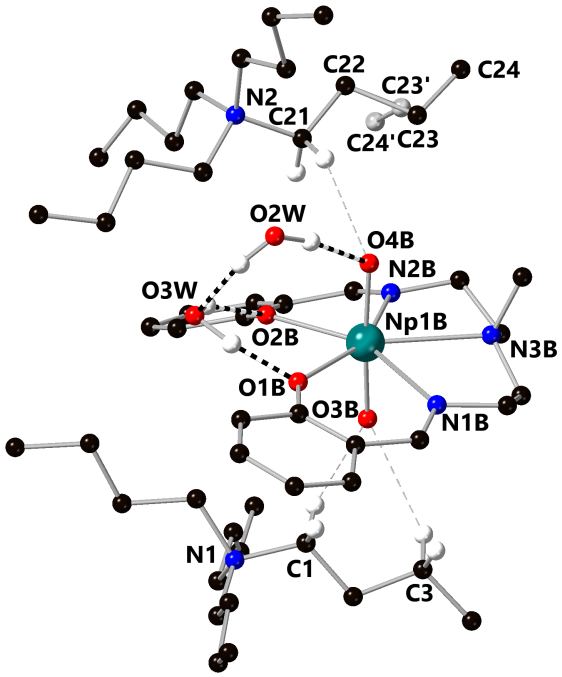

Figure S56: Molecule B of $\mathbf{[NpO_2L^{NM}]^- \cdot 2.5H_2O}$ (m36a) and the tetrabutylammonium ions that interact with it in the solid-state. Hydrogen bonding interactions are denoted with bold dashed lines and weak electrostatic interactions with the NpO_2^+ cores are denoted with gray dashed lines. Molecule A, disordered atoms, and all hydrogen atoms except those engaged in the noted interactions are omitted for clarity.

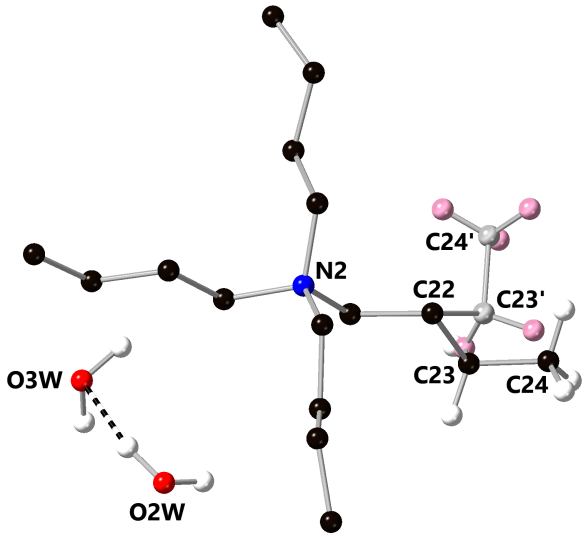

Figure S57: Disorder model of the tetrabutylammonium cation containing N2. The major orientation is denoted C22, C23, and C24 while the minor orientation is shown in lighter color atoms and denoted C22', C23', and C24'. Molecules A and B, the tetrabutylammonium ion containing N1, and all other hydrogen atoms are omitted for clarity.

5.3 Special Refinement Details for $[NpO_2L^{NM}]^- \cdot 3H_2O$ (m61a)

The structure of $[NpO_2L^{NM}]^- \cdot 3H_2O$ (m61a) crystallizes in the triclinic space group $P\bar{1}$ and the asymmetric unit contains crystallographically independent Np sites in two molecules of $[NpO_2L^{NM}]^-$, two tetrabutylammonium counter cations, two fully occupied water molecules, and two partially-occupied water molecules. All aromatic and aliphatic protons were incorporated into the structural model as sp^3-hybridized riding model groups. Protons positions on O1W, O2W, O3W, and O4W were not located in the difference map and thus were refined to idealized positions then fixed.

While the tetrabutylammonium cation containing N2 and C17-C32 is well-ordered, a disorder model was applied to one butyl chain in the tetrabutylammonium cation containing N1 and C1-C16. Specifically, atoms C14-C16 were modeled as being disordered over two positions in a 56/44(1) fashion (the minor orientation is denoted C14'-C16'). The bond lengths and tetrahedral bond angles for C14-C16 and C14'-C16' were restrained to appropriate multiples of the C–C bond length that was included in the refinement as a free variable which refined to a final value of 1.483(8) Å; this is reasonable considering the expected C–O bond length is 1.513 Å.[4] Finally, moderate restraints were applied to the anisotropic displacement parameters of C6, C7, C8, C11, C12, N3B, C16B, C17B, C14', C15', C16', C22, C23, and C24, in the form of ISOR and SIMU commands.

Moderate-strength hydrogen bonding interactions can be measured between the co-crystallized water molecule O1W and molecule A with donor-acceptor distances of 2.546(12) Å for O1W$\cdots$O1A, 2.944(12) Å for O1W$\cdots$O2A, and 2.816(8) Å for O3W$\cdots$O4A.[5]

Molecule B engages in similar moderate-strength hydrogen bonding interactions with O2W and O3W with donor-acceptor distances of 2.877(15) Å for O2W$\cdots$O4B, 2.822(8) Å for O4W$\cdots$O1B, and 2.814(7) Å for O4W$\cdots$O2B.[5]

Finally, weak electrostatic interactions between the tetrabutylammonium cations and both molecules of $[NpO_2L^{NM}]^- \cdot 3H_2O$ (m61a) throughout the structure. Donor-acceptor

distances for these interactions are given in Table S4.

Table S4: Donor-acceptor distances for the weak electrostatic interactions measured in **[NpO_2L^{NM}]$^-$·3H_2O** (m61a).

Donor-acceptor pair	Distance (Å)
C17···O3A	3.060(8)
C19···O3A	3.359(9)
C18A···O4A	3.368(9)
C21···O3B	3.180(10)
C29···O4W	3.290(9)
C9···O4B	3.252(10)

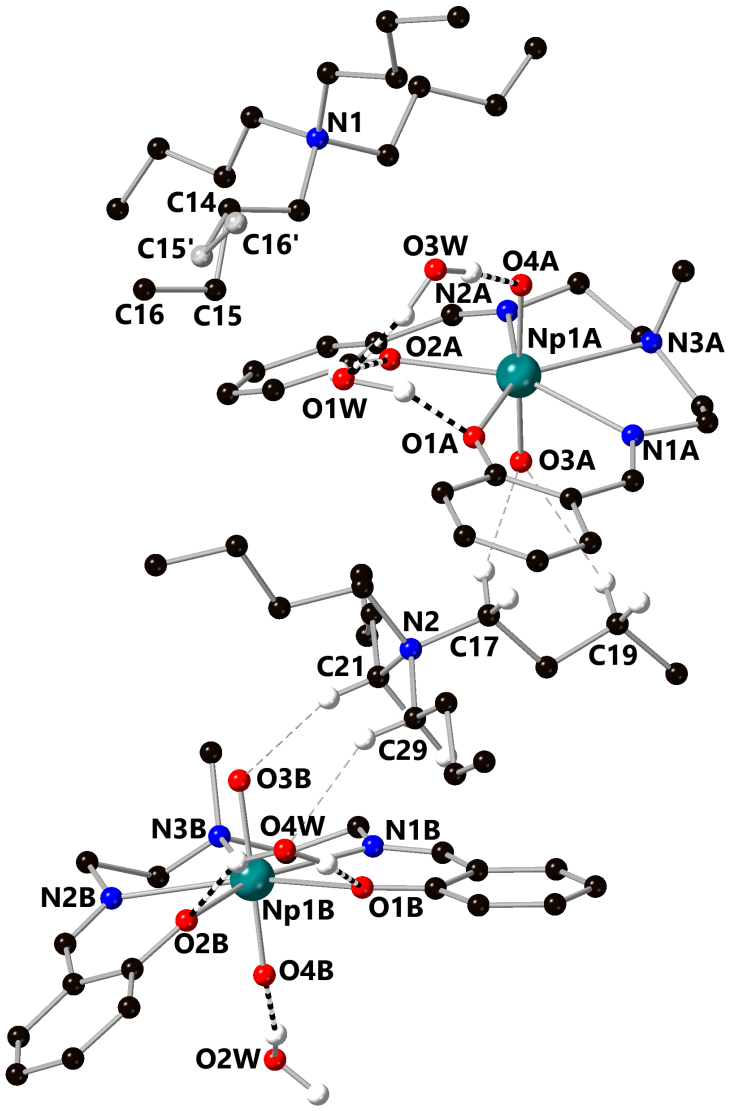

Figure S58: Ball and stick representation of the asymmetric unit of $\mathbf{[NpO_2L^{NM}]^- \cdot 3H_2O}$ (m61a). Hydrogen bonding interactions are denoted with bold dashed lines and weak electrostatic interactions with the NpO_2^+ cores are denoted with gray dashed lines. All hydrogen atoms except those engaged in the noted interactions are omitted for clarity and disordered atoms are shown in gray.

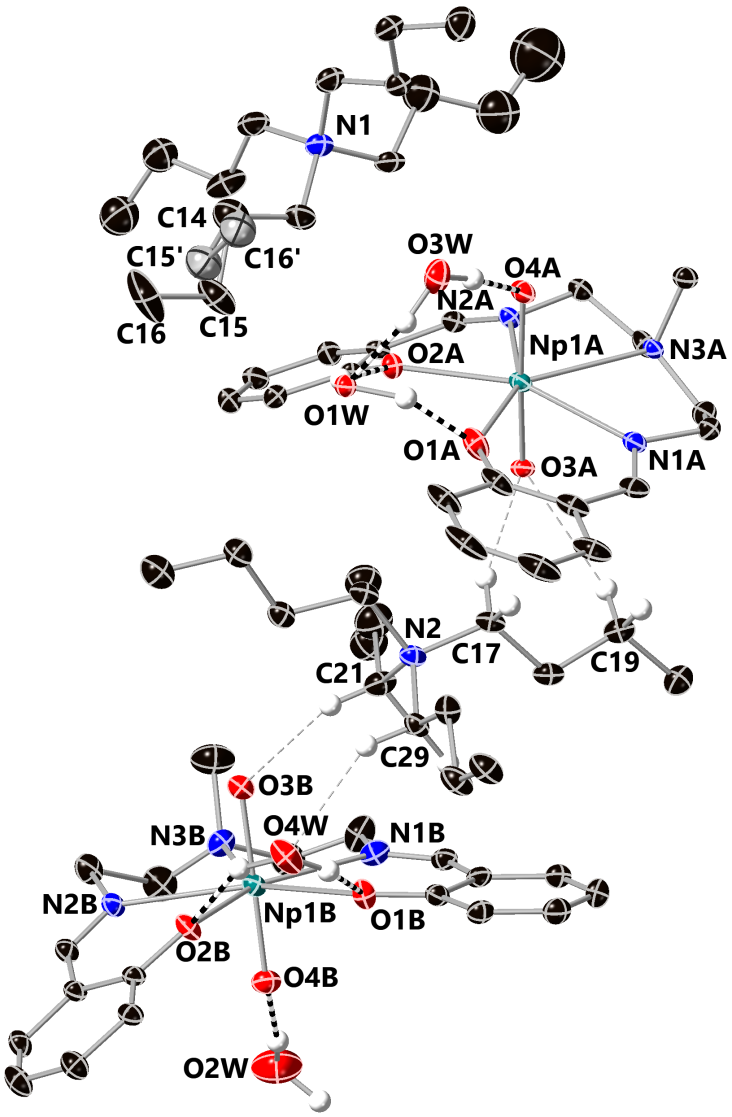

Figure S59: Asymmetric unit of $\mathbf{[NpO_2L^{NM}]^- \cdot 3H_2O}$ (m61a). Hydrogen bonding interactions are denoted with bold dashed lines and weak electrostatic interactions with the NpO_2^+ cores are denoted with gray dashed lines. All hydrogen atoms except those engaged in the noted interactions are omitted for clarity and disordered atoms are shown in gray. Displacement ellipsoids are shown at the 20% probability level.

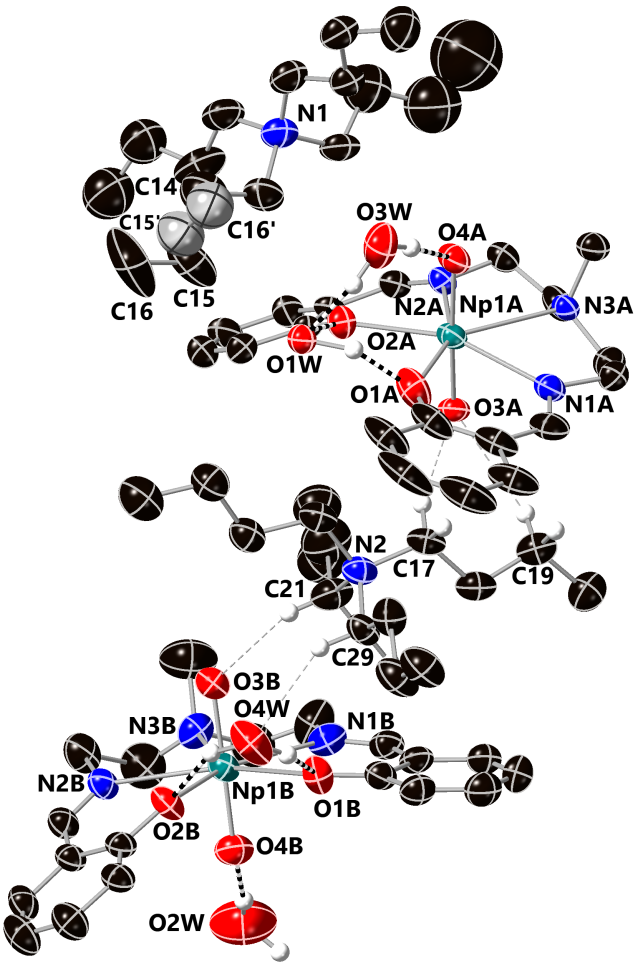

Figure S60: Asymmetric unit of $\mathbf{[NpO_2L^{NM}]^- \cdot 3H_2O}$ (m61a). Hydrogen bonding interactions are denoted with bold dashed lines and weak electrostatic interactions with the NpO_2^+ cores are denoted with gray dashed lines. All hydrogen atoms except those engaged in the noted interactions are omitted for clarity and disordered atoms are shown in gray. Displacement ellipsoids are shown at the 50% probability level.

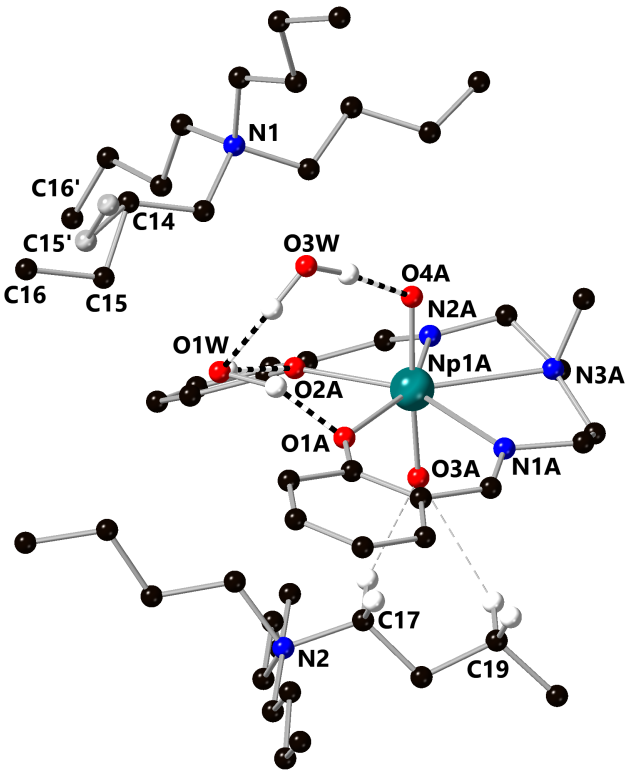

Figure S61: Molecule A of $\mathbf{[NpO_2L^{NM}]^- \cdot 3H_2O}$ (m61a) and the tetrabutylammonium ions that interact with it in the solid-state. Hydrogen bonding interactions are denoted with bold dashed lines and weak electrostatic interactions with the NpO_2^+ cores are denoted with gray dashed lines. Molecule B and all hydrogen atoms except those engaged in the noted interactions are omitted for clarity.

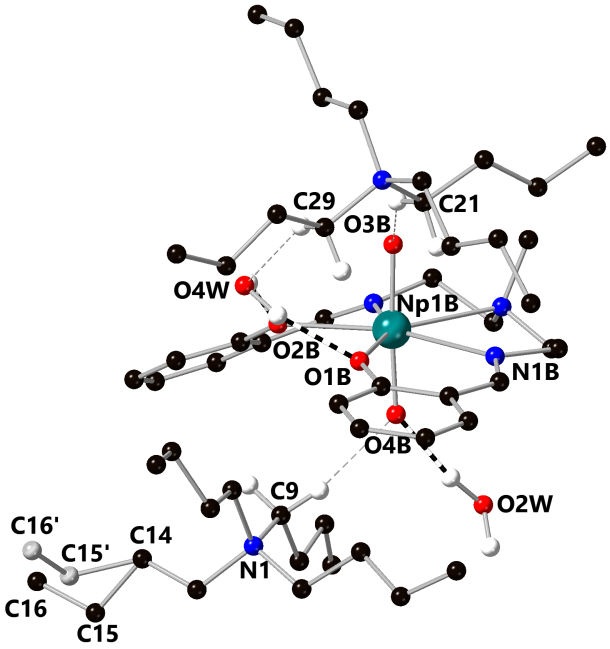

Figure S62: Molecule B of $\mathbf{[NpO_2L^{NM}]^-{\cdot}3H_2O}$ (m61a) and the tetrabutylammonium ions that interact with it in the solid-state. Hydrogen bonding interactions are denoted with bold dashed lines and weak electrostatic interactions with the NpO_2^+ cores are denoted with gray dashed lines. Molecule A, disordered atoms, and all hydrogen atoms except those engaged in the noted interactions are omitted for clarity.

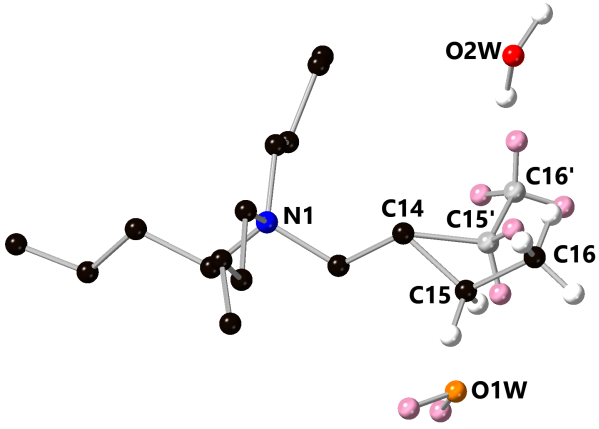

Figure S63: Disorder model of the tetrabutylammonium cation containing N1 and the two partially occupied water molecules O2W and O1W. The position of O2W is linked to the positions of C14, C15, and C16, while the position of O1W is linked to C14', 15', and C16'. The minor disorder orientation is shown in lighter atom colors. Molecules A and B, the tetrabutylammonium ion containing N2, and all other hydrogen atoms are omitted for clarity.

Table S5: Crystallographic parameters for $\mathbf{[NpO_2L^{NM}]^-\cdot 3H_2O}$ (m60a), $\mathbf{[NpO_2L^{NM}]^-\cdot 2.5H_2O}$ (m36a), and $\mathbf{[NpO_2L^{NM}]^-\cdot 3H_2O}$ (m61a).

	m60a	**m36a**	**m61a**
Molecular Formula	$C_{70}H_{120}N_8Np_2O_{11}$	$C_{140}H_{234}N_{16}Np_4O_{21}$	$C_{70}H_{120}N_8Np_2O_{11}$
CCDC accession code	2373058	2379285	2379286
F.W. (g/mol)	1723.73	3425.42	1723.73
Color	green	green	green
Temperature(K)	293(2)	100(2)	293(2)
MoK$_\alpha$ (Å)	0.71073	0.71073	0.71073
Crystal System	triclinic	triclinic	triclinic
Space Group	P$\bar{1}$ (No. 2)	P$\bar{1}$ (No. 2)	P$\bar{1}$ (No. 2)
a (Å)	9.9425(8)	9.9804(7)	9.9521(4)
b (Å)	18.0802(15)	18.0918(13)	18.0582(8)
c (Å)	21.1419(17)	21.0492(15)	21.1643(9)
α (deg.)	93.5480(10)	93.7700(10)	93.5620(10)
β (deg.)	98.0660(10)	98.4830(10)	97.9810(10)
γ (deg.)	94.4730(10)	94.1060(10)	94.4390(10)
Vol. (Å^3)	3741.2(5)	3738.2(5)	3745.2(3)
Z	2	1	2
ρ_{calc} (g/cm^3)	1.530	1.522	1.529
μ (mm^{-1})	2.822	2.824	2.819
F(000)	1740	1726	1740
Theta range	1.95 to 53.16°	2.26 to 55.11°	2.27 to 54.21°
Index ranges	-12 $\leq$ h $\leq$ 12	-12 $\leq$ h $\leq$ 12	-12 $\leq$ h $\leq$ 12
	-22 $\leq$ k $\leq$ 22	-23 $\leq$ k $\leq$ 23	-23 $\leq$ k $\leq$ 23
	-26 $\leq$ l $\leq$ 26	-27 $\leq$ l $\leq$ 27	-27 $\leq$ l $\leq$ 27
Reflections collected	45606	33158	48307
Independent reflections	15554	17116	16536
	[R_{int} = 0.0555,	[R_{int} = 0.0455,	[R_{int} = 0.0644,
	R_{sigma} = 0.0642]	R_{sigma} = 0.0781]	R_{sigma} = 0.0775]
Completeness/θ_{max}	99.9%/25.242°	99.9%/25.242°	100%/25.242°
Absorption correction	Multi-scan	Multi-scan	Multi-scan
Max./Min. Transmission	1.454	2.664	1.470
Data/restraints/parameters	15556/60/859	17116/120/851	16536/103/859
Goodness-of-fit on f^2	1.030	1.130	1.016
Final R indices [I $\geq 2\sigma$(I)]	R_1 = 0.0524	R_1 = 0.0477	R_1 = 0.0534
	wR_2 = 0.1207	wR_2 = 0.0846	wR_2 = 0.1155
R indicies (all data)	R_1 = 0.0782	R_1 = 0.0981	R_1 = 0.0879
	wR_2 = 0.1354	wR_2 = 0.0968	wR_2 = 0.1307
Largest diff peak & hole (e Å^{-3})	2.00/-1.42	1.46/-0.82	2.00/-1.05

References

(1) Anson, F. C. Innovations in the Study of Adsorbed Reactants by Chronocoulometry. *Anal. Chem.* **1966**, *38*, 54–57.

(2) Golwankar, R. R.; Makos, M. Z.; Gajiao, N.; Neidig, M. S.; Oliver, A. G.; Day, C. S.; Day, V. W.; Glezakou, V.-A.; Blakemore, J. D. Electrochemical Activation and Functionalization of the Uranyl Ion. *ChemRxiv* **2023**, *doi: 10.26434/chemrxiv-2023-gnbpd*.

(3) Mikeska, E. R.; Wilson, R. E.; Blakemore, J. D. PCET-driven Reactivity of Neptunyl(VI) Yields Oxo-bridged Np(V) and Np(IV) Species. *ChemRxiv* **2024**, *doi: 10.26434/chemrxiv-2024-3rrhz*.

(4) Allen, F. H.; Watson, D. G.; Brammer, L.; Orpen, A. G.; Taylor, R. *Typical interatomic distances: organic compounds. In International Tables for Crystallography, Vol. C*; International Union of Crystallography, 2006; pp 790–811.

(5) Jeffrey, G. A. *An Introduction to Hydrogen Bonding*; Oxford University Press: New York, NY, 1997; p 12.